BNL-112499-2016-JA

A HYBRID METHOD TO ESTIMATE SPECIFIC DIFFERENTIAL PHASE AND RAINFALL WITH LINEAR PROGRAMMING AND PHYSICS CONSTRAINTS

Hao Huang, Guifu Zhang, Kun Zhao, and Scott E. Giangrande

Accepted for publication in
IEEE Trans. Geosci. Remote Sensing

July 2016

Environmental & Climate Science Dept.

Brookhaven National Laboratory

U.S. Department of Energy
USDOE Office of Science (SC),
Basic Energy Sciences (BES) (SC-22)

DISCLAIMER

A Hybrid Method to Estimate Specific Differential Phase and Rainfall with Linear Programming and Physics Constraints

Hao Huang[1], Guifu Zhang[1,2], Kun Zhao[1], and Scott E. Giangrande[3]

1: School of Atmospheric Science, Nanjing University, Nanjing, Jiangsu, China

2: School of Meteorology, University of Oklahoma, Norman, Oklahoma, USA

3: Environmental and Climate Sciences Dept., Brookhaven National Laboratory, Upton, New York, USA

Abstract

A hybrid method of combining linear programming and physical constraints is developed to estimate specific differential phase (K_{DP}) and to improve rain estimation. The hybrid K_{DP} estimator, and the existing estimators of linear programming (LP), least square fitting (LSF), and a self-consistent (SC) relation of polarimetric radar variables are evaluated and compared using simulated data. Simulation results indicate the new estimator's superiority, especially in regions where backscattering phase (δ_{hv}) dominates. Furthermore, quantitative comparison between auto weather station (AWS) rain gauge observations and K_{DP}-based radar rain estimates for a Meiyu event also demonstrate the superiority of the hybrid K_{DP} estimator over existing methods.

1. Introduction

In recent years, the dual-polarization upgrade of weather radar networks has yielded new measurements and information that provide valuable new insights into cloud and precipitation processes over conventional weather radar observations. In addition to the radar reflectivity factor (Z_{H}), polarimetric radars measure several new quantities including the differential reflectivity factor (Z_{DR}), specific differential phase (K_{DP}), and co-polar cross-correlation coefficient (ρ_{hv}) [1]. These polarimetric measurements, when used alone or in combination, help to significantly improve hydrological applications including quantitative precipitation estimation (QPE) [2, 3]. In particular, the inclusion of K_{DP}, defined as the range derivative of the differential propagation phase (ϕ_{DP}) between the two polarized signals, offers many advantages for QPE, especially in challenging heavier rainfall contexts [4]. Specifically, K_{DP} is better correlated with the rainrate R at all weather radar frequencies and is immune to radar mis-calibration, attenuation in precipitation, and partial beam blocking. Furthermore, K_{DP} has been successfully applied within bulk hydrometeor classification routines since it is uniquely sensitive to improve the designation of graupel and dendritic snow crystals [5].

Despite these known advantages for QPE, there are still issues in obtaining accurate K_{DP} estimates from the polarimetric radar measured differential phase (Φ_{DP}). Typically, K_{DP} is estimated from the range derivative of the measured (Φ_{DP}). However, the measured differential phase Φ_{DP} is composed of the differential propagation phase (ϕ_{DP}), differential backscattering phase (δ_{hv}), and measurement errors including statistical/sampling error, ground clutters, side lobes, second-trip echoes, mixed-phase hydrometeors (large melting aggregates and hailstones), non-uniform beam filling and so on [6-8]. This may be expressed as, $\Phi_{\mathrm{DP}} = \phi_{\mathrm{DP}} + \delta_{\mathrm{hv}} + \varepsilon$ if ignoring certain error contributions from ground clutter, side lobes, non-uniform beam filling, etc. Contributions from these terms can be mostly removed in the quality control procedure. To reduce effects of statistical errors ε, it is useful to smooth Φ_{DP} so that the range derivative of ϕ_{DP} can be correctly calculated. Nevertheless, excessive smoothing of Φ_{DP} results in overly processed K_{DP} estimates that lose fine-scale precipitation features. For shorter wavelength radars and applications (e.g., X-band and C-band, with 3-cm and 5-cm wavelengths, respectively), the δ_{hv} may also contribute large errors to K_{DP} estimation [4]. Therefore, it is increasingly critical at shorter wavelengths to separate ϕ_{DP} contributions from Φ_{DP} accurately to reduce the error in ϕ_{DP} for K_{DP} estimation, while keeping the inherent spatial structure of precipitation.

Many algorithms have been proposed towards obtaining accurate K_{DP} estimates from Φ_{DP}. One common method is to apply various forms of signal filters, such as FIR filter [9, 10] or wavelet analysis [11]. In these approaches, high frequency components along the Φ_{DP} radial measurement profiles are removed. The most basic approach has been to fit noisier Φ_{DP} radial profiles with a smoothed one based on a median filter, a moving average, or more sophisticated averaging methods. Recently, an algorithm based on a Kalman filter approach was also proposed, suggesting improved estimation accuracy under lower signal-to-noise ratio (SNR) conditions [12].

Since δ_{hv} contributions are typically less significant at the longer wavelengths in rain media (e.g., S-band, 10-cm wavelength), the operational dual-polarization WSR-88D network is able to implement a simple, least-square fitting (LSF) method. For these radars, K_{DP} is estimated by applying LSF on multiple gates of Φ_{DP} measurements over adaptive radial ranges. These filter lengths vary from approximately 2 to 6 kilometers, based on the intensity of radar echo (Z_{H}), centered on that range gate [13]. This approach selects Φ_{DP} data filtered over a relatively large radial range (6 km) for the moderate-to-weak echo $Z_{\mathrm{H}} < 40$ dBZ), and over a relatively small radial range (2 km) for strong echo ($Z_{\mathrm{H}} > 40$ dBZ). The advantage of this adaptive range, or 'synthetic' solution, is that it is simple to implement operationally. The approach reflects a compromise that prevents K_{DP} from being overly smoothed in severe convective regions, while facilitating rainfall rate estimation by heavily smoothing within light precipitation regions where K_{DP} estimates are typically noisier.

Due to the fact that the sampling volume averaged axis ratio (ratio of minor axis and major axis) of raindrops is never larger than 1 [2, 14], intrinsic K_{DP} is nonnegative when the radar beam goes through liquid hydrometers. Nevertheless, the aforementioned estimation methods will occasionally produce negative K_{DP} estimates in rain due to contributions from the backscattering phase δ_{hv}, nonuniform beam filling, or other statistical errors of Φ_{DP} measurements [15]. As K_{DP} estimates should be unbiased by δ_{hv} at the longer wavelengths, Ryzhkov and Zrnic proposed to incorporate negative rainfall rate values into spatiotemporal integrals, such as using a formula

$R = 40.6|K_{DP}|^{0.866}\,\mathrm{sign}(K_{DP})$ [8]. Similarly, to designate or better account for the role of negative K_{DP} values on hydrological applications including those originating from backscattering phase or other contributions, it is useful to examine statistical K_{DP} - Z_H relationships and replace physically unrealistic, negative K_{DP} estimates with physically realistic values estimated from Z_H. Simply adopting the latter approach, K_{DP} and K_{DP}-based rain rate estimates may appear cosmetically more accurate, especially at the rear or peripheral gradient regions of intense storms wherein negative K_{DP} regions are the most prominent. However, the ramifications for such substitutions are statistically important, since artificial negative K_{DP} excursions are accompanied by artificial positive K_{DP} excursions. Therefore, the radial integral of K_{DP}, which is related to ϕ_{DP}, would significantly increase due to the simple replacement of negative K_{DP}, leading to an overestimation for the total accumulated rainfall from K_{DP}-based rainrate spatiotemporal integrals. Several methods including so-called 'ZPHI' methods have been suggested to offset several of these concerns by constraining the substitutions according to the path integrated differential phase [16]

Recently, a linear programming (LP) method [17] has been proposed that may mitigate the Φ_{DP} noisiness and improve K_{DP} estimation simultaneously. The LP method is mainly based on linear optimization theory [18]. The basis for the method was to extract a ϕ_{DP} curve that best minimizes the difference between this extracted curve and the measured Φ_{DP} at a given series of linear constraints. For the initial proof-of-concept article, the assumption for nonnegative K_{DP} values served as an example constraint set

[17]. Using simulated and real datasets, the approach indicated nonnegative K_{DP} estimates, monotonously increasing ϕ_{DP}, and unbiased accumulated rainfall estimation with better fine-tuned range distribution over conventional methods. Moreover, simplified self-consistency constraints such as $K_{\mathrm{DP}} = aZ_{\mathrm{H}}{}^{b}$ were identified as possible means to further improve and constrain these methods, but were not well-developed in that study.

As highlighted by Giangrande et al. [17], Ryzhkov and Zrnic [8] and many others, relationships between K_{DP} and Z_{H} are commonly used to identify and adjust unreasonable K_{DP} values (or partial beam blockages in Z_{H}) since both measurements are related to rainfall intensity. However, K_{DP} and Z_{H} are approximately the 4.2$^{\mathrm{nd}}$ and 6$^{\mathrm{th}}$ moments of DSD, respectively [1, 4], thus their relationship is nonlinear, unstable and easily affected by the variability of the raindrop size distributions (DSD). Self-consistent (SC) relations as proposed by Scarchilli [19], Vivekanandan [20], Giangrande [21] have shown that Z_{H}, Z_{DR} and K_{DP} triplets reside within a limited and possibly exploitable three-dimensional space for rainfall studies, more stable than two-parameter K_{DP} - Z_{H} relations and are less affected by raindrop size distribution (DSD) variability. By using well-calibrated and attenuation-corrected Z_{H} and Z_{DR}, it is possible to estimate K_{DP} from the self-consistency of polarimetric radar data (PRD). It can be expected that this estimation is always non-negative and close to the intrinsic values. Unless highly contaminated by hail presence, the self-consistent relations are useful information to be utilized in K_{DP} estimation.

Moreover, algorithms such as LSF, LP and those benefitting from self-consistency have advantages and disadvantages. Therefore, this study is motivated by an attempt to combine the best attributes of those methods into a more optimal approach for K_{DP} estimation. In order to make use of as much information provided by polarimetric measurements as possible, we propose a hybrid method to estimate K_{DP} in rain regions that combines the strengths of LSF and SC under an enhanced LP framework. This paper is organized as follows. Section 2 describes the methodology and implementation associated with the LSF, simplified LP, and basic SC approach. Section 3 presents an ideal experiment and a comparison of the results from these algorithms. In Section 4, an enhanced LP hybrid method that better incorporates these three concepts is proposed and applied on the ideal case to show its advantages. A qualitative and a quantitative comparison of basic LSF, simple LP and enhanced LP hybrid methods during a Meiyu event are present in Section 5. Finally, a summary and some discussions on future work are given in Section 6.

2. Methodology

According to the textbook definition for K_{DP} [4], only Φ_{DP} measurements from two range gates are needed to obtain the intrinsic value, as in formula $K_{\mathrm{DP}} = \dfrac{\phi_{\mathrm{DP}}(r_2) - \phi_{\mathrm{DP}}(r_1)}{2(r_2 - r_1)}$, provided there are no errors in Φ_{DP} measurements, i.e., Φ_{DP} is identical to intrinsic ϕ_{DP}.

When errors exist in the measurements, this problem becomes ill-posed. Retrieving K_{DP} according to its definition would lead to an unpractical result, especially when statistical errors of Φ_{DP} are relatively large. Fortunately, in weather systems and associated storm-scale research, precipitation regimes and DSD properties does not change significantly from gate to gate. Because of this, measurements of more than two gates are often used to determine the K_{DP}. This estimation becomes over-determined when multiple measurements are involved in evaluating one variable [22]. All the aforementioned methods concern the issue of solving this over-determined system and obtaining outcomes close to the intrinsic values. The K_{DP} estimation methods of LSF, LP and self-consistency are reviewed in this section.

A. Least Square Fitting

Least square fitting is a common regression approach to obtain approximate solutions for an over-determined system. When the K_{DP} of an intermediate range gate needs to be determined; multiple Φ_{DP} measurements (with errors) from the gates adjacent along the radial construct the whole system. Generally, the number of gates to be included should be determined mainly according to the standard deviation of the errors, which depends on the signal noise ratio (or SNR) of the radar data, estimation error of Φ_{DP}, and the variability of K_{DP} along the radial. As employed by the WSR-88D radar and CSU–CHILL radar [23] systems, we apply piecewise LSF on adaptive lengths with respect to echo intensity, i.e., Z_{H}. Two sets of experiments with different adaptive lengths are run to examine the dependence of LSF on the filter lengths in the next section.

One experiment uses the same adaptive lengths as those used by WSR-88D, i.e., 2 km (6 km) for gates where Z_{H} is beyond (below) 40 dBZ. The other one uses the twice of the WSR-88D adaptive lengths. The LSF formula is applied on Φ_{DP} measurements at the gates within the adaptive lengths to obtain the K_{DP} estimate at the intermediate gate:

$$K_{\mathrm{DP}} = \frac{\sum_{i=1}^{n}\left\{[\Phi_{\mathrm{DP}}(i) - \bar{\Phi}_{\mathrm{DP}}]\bullet[r(i) - \bar{r}]\right\}}{2\sum_{i=1}^{n}[r(i) - \bar{r}]^2}, \tag{1}$$

where the overbar "$-$" means an averaged value, and r is the distance of Φ_{DP} measurements from the radar.

B. Linear Programming

As proposed by Giangrande et al. [17], results from the LP with nonnegative constraints are summarized as follows. The main idea is optimizing ϕ_{DP} under the physical constraints of rain. We denote the n-gate raw differential phase ray with $\mathbf{b} = (b_1, b_2, \cdots, b_n)$ and the filtered or processed ray with $\mathbf{x} = (x_1, x_2, \cdots, x_n)$, respectively. The LP problem is set as minimizing the difference between $\mathbf{b}$ and $\mathbf{x}$, i.e. $\mathrm{f} = \sum_{i=1}^{n}|x_i - b_i|$. To mathematically deal with the absolute value, an intermediate vector $\mathbf{z} = (z_1, z_2, \cdots, z_n)$ is introduced that represents the variables that appear in the cost function. Regardless of whether $x_i - b_i$ is positive, negative or zero, $z_i \geq |x_i - b_i|$ is always equivalent to the combination of two inequalities $z_i \geq x_i - b_i$ and $z_i \geq b_i - x_i$. Now the minimization of f becomes the minimization of the n-term cost function $\sum_{i=1}^{n} z_i$ under two sets of constraints, $z_i - x_i \geq -b_i$ and $z_i + x_i \geq b_i$. Mathematically, we let $\mathbf{x}_\mathrm{c} = (\mathbf{z}, \mathbf{x})^\mathrm{T}$ be the independent variable of the LP problem. Now, the cost function $\sum_{i=1}^{n} z_i$, i.e., sum of the elements of $\mathbf{z}$, can be rewritten as a dot product, $\mathbf{c} \bullet \mathbf{x}_\mathrm{c}$, with the coefficient vector expressed as $\mathbf{c} = (1_1,\ \cdots,\ 1_n,\ 0_{n+1},\ \cdots,\ 0_{2n})$. It was noted by Giangrande et al. [17] that potential missing data in the observations can be handled by setting the weights of the corresponding gates to zeros.

The matrix–vector form of the LP problem becomes minimizing $\mathbf{c} \bullet \mathbf{x}_\mathrm{c}$ under the constraint of $\mathbf{A}\mathbf{x}_\mathrm{c} \geq \mathbf{b}$, in which $\mathbf{A} = \begin{pmatrix} \mathbf{I}_n & -\mathbf{I}_n \\ \mathbf{I}_n & \mathbf{I}_n \end{pmatrix}$, and $\mathbf{I}_n$ is the $n \times n$ identity matrix. If there are no other constraints, the cost function reduces to zero when $\mathbf{x}$ equals to $\mathbf{b}$. When we add a nonnegative K_DP constraint to the LP problem as in Giangrande et al. [17], a $(n - \frac{m-1}{2}) \times n$ matrix $\mathbf{M}_{n-(m-1)/2,\, n}$ is employed to convert the filtered differential phase to its derivative, K_DP. The matrix $\mathbf{M}_{n-(m-1)/2,\, n}$ is composed of coefficients of the m-point Savitzky–Golay (S-G) second-order polynomial derivative filter:

$$C_\text{S-G}(i) = \frac{6(2i - m - 1)}{m(m+1)(m-1)},\ i = 1,\ 2,\ \cdots,\ m, \tag{2}$$

yielding,

$$\mathbf{M}_{n-(m-1)/2,\,n}=\begin{pmatrix} C_{\text{S-G}}(1) & \cdots & C_{\text{S-G}}(m) & 0_{m+1} & 0_{m+2} & \cdots & 0_{n} \\ 0_{1} & C_{\text{S-G}}(1) & \cdots & C_{\text{S-G}}(m) & 0_{m+2} & \cdots & 0_{n} \\ & \cdots & & & & \cdots & \\ 0_{1} & \cdots & 0_{n-m-1} & C_{\text{S-G}}(1) & \cdots & C_{\text{S-G}}(m) & 0_{n} \\ 0_{1} & \cdots & 0_{n-m-1} & 0_{n-m} & C_{\text{S-G}}(1) & \cdots & C_{\text{S-G}}(m) \end{pmatrix},\quad (3)$$

where 0_j means zero at the j^{th} column. With the m-point derivative filters involved, K_{DP} array can be expressed as $\mathbf{M}_{n-(m-1)/2,\,n}\mathbf{x}^{\text{T}}$. The linear inequality $\mathbf{M}_{n-(m-1)/2,\,n}\mathbf{x}^{\text{T}} \geq \mathbf{Z}_{n-(m-1)/2}$ serving as the nonnegative K_{DP} constraint can be merged into the now augmented parts of matrix-vector form of the LP problem, in which $\mathbf{Z}_{n-(m-1)/2}$ is a zero vector. The modified algebraic form is now minimizing $\mathbf{c}\bullet\mathbf{x}_{\text{c}}$ under the constraint of $\mathbf{A}_{\text{AUG}}\mathbf{x}_{\text{c}} \geq \mathbf{b}_{\text{AUG}}$, which is the combination of the minimization and nonnegative constraint. The augmented matrix $\mathbf{A}_{\text{AUG}}$ and vector $\mathbf{b}_{\text{AUG}}$ can be expressed as:

$$\mathbf{A}_{\text{AUG}}=\begin{pmatrix} \mathbf{I}_{n} & -\mathbf{I}_{n} \\ \mathbf{I}_{n} & \mathbf{I}_{n} \\ \mathbf{Z}_{n-(m-1)/2,n} & \mathbf{M}_{n-(m-1)/2,n} \end{pmatrix}, \quad (4)$$

$$\mathbf{b}_{\text{AUG}}=\left(-\mathbf{b},\mathbf{b},\mathbf{Z}_{n-(m-1)/2}\right)^{\text{T}}, \quad (5)$$

respectively, where $\mathbf{Z}_{n-(m-1)/2,\,n}$ is a zero matrix. Many toolkits have been developed to solve LP problems [24, 25]. It is noted that, SciPy [26] provides a very convenient way to obtain a satisfactory solution $\mathbf{x}_{\text{c}}$. K_{DP} estimates are obtained from the formula $\mathbf{K}_{\mathbf{DP}}=\mathbf{M}_{n-(m-1)/2,n}\mathbf{x}^{\text{T}}$, in which $\mathbf{x}$ should be preprocessed with a smoothing filter.

It seems at first glance that the LP estimation system is a well-posed linear system when applied on the K_{DP} estimation problem, because the numbers of measurements (Φ_{DP}) and state variables (K_{DP} or ϕ_{DP} in this particular system) are the same. Yet, mathematically it will lead to a meaningless solution because of observation errors. However, the underlying principle is that, each m-point S-G derivative filter in $\mathbf{M}_{n-(m-1)/2,\,n}\mathbf{x}^{\mathrm{T}}$ connects ϕ_{DP} of m gates with K_{DP} at the intermediate gate. This is an analogy to an LSF within each adaptive range. It is worth noting that adaptive derivative filters cannot be applied in the LP estimation method. These derivative filters act as a constraint of state variable ϕ_{DP}. If the lengths of the filters vary, ϕ_{DP} would not be monotonous. This study does not further explore this problem. For the purpose of manifesting the effect of the S-G derivative filter, the results from the LP method with derivative filters of 2 km and 6 km lengths are shown.

C. Self-consistency

Previous studies have shown that the intrinsic K_{DP} values are constrained well by the intrinsic Z_{H} and Z_{DR} [19-21]. Although the simple SC relation $K_{\mathrm{DP}} = aZ^{b}$ was identified as one possibility to set a threshold in the LP method [17], the usage of self-consistency was not thoroughly studied for K_{DP} or rainfall estimation, with emphasis on shorter wavelengths wherein such constraints are more beneficial [27]. In order to obtain the intrinsic self-consistent relation, polarimetric radar variables should be calculated from in-situ observations (DSD data in this case). The T-matrix method can be used to compute scattering amplitude of raindrops at different sizes [28, 29]. With knowledge of the scattering amplitude, a PRD could be calculated [1]. Since the DSD characteristics may change for different cases, it is better to use climatological DSD observations to obtain a robust self-consistent relation among the polarimetric variables, which is expressed by

$$K_{\mathrm{DP}}(Z_{\mathrm{h}}, Z_{\mathrm{dr}}) = C Z_{\mathrm{h}}^{\alpha} Z_{\mathrm{dr}}^{\beta}, \quad (6)$$

where Z_{h} and Z_{dr} are the linear forms of Z_{H} and Z_{DR}. The parameters C, α and β can be estimated by minimizing the sum of the squared errors of Z_{h}, Z_{dr} and K_{DP} from the equation. K_{DP} estimates can be acquired from measured Z_{H} and Z_{DR} with Eq. (6). It is noteworthy that Z_{H} and Z_{DR} measurements suffer from attenuation in rain, mis-calibration, partial beam blockages and random fluctuations. Mis-calibration, partial beam blockages and attenuation should be corrected first [30-33], or corrected adaptively. The impact of random fluctuations can be reduced by applying moving median and mean filters.

In this method, the errors of K_{DP} estimates are attributed to the inaccuracy (or, lack of representativeness) of the self-consistent relation and the errors of measurements (i.e., Z_{H}, Z_{DR}). A detailed error analysis is worthwhile, but beyond the scope of this paper. Estimates from self-consistency method with two different $Z_{\mathrm{H}} / Z_{\mathrm{DR}}$ moving filters are compared in the next section.

3. Ideal Experiment

A. Experiment Design

LSF, LP and SC based K_{DP} estimation methods are applied on a set of radial simulated PRD to illustrate the different characteristics of each method. These simulated PRD are based on a time series of DSD observation from a 2-D video disdrometer (2DVD), which is deployed at Nanjing City, Jiangsu Province in Eastern China, from a precipitation event on July 19, 2015. The position of the 2DVD is denoted on the topographic map in Fig. 1.

A constrained gamma model is used to process the DSD observations to generate the simulated data [34, 35], which is expressed by

$$N(D) = N_0 D^{\mu} \exp(-\Lambda D), 0 \le D \le D_{\max}, \tag{7}$$

where $N(D)$ is the raindrop number concentration of each size interval; D is the equivalent volume diameter (unit [mm]); $D_{\max}$ is the maximum equivalent diameter of raindrops and is assumed to be 8.0 mm; N_0 is the number concentration parameter; μ is the shape parameter; and $\Lambda(\mathrm{mm}^{-1})$ is another parameter of distribution. Since the constrained gamma model uses a statistical relation between the parameters μ and Λ, only two estimated DSD moments are needed to find the DSD parameters in (7).

First, the 3rd (M_3) and 6th (M_6) moments of the DSD

$$M_n = \int_0^{D_{\max}} D^n N(D)\, dD, \tag{8}$$

are estimated from observations [36]. A moving median and mean filter are used to filter out the high frequency fluctuations of moments. These fluctuations are mostly caused by the micro-scale variability of precipitation systems, the difference of sampling volume between disdrometer and radar, and the observation errors of disdrometer. After this procedure, M_3 and M_6 are linearly interpolated so that the simulated data can have a radial resolution of 75 meters. We then use a method similar to the truncated moment fit method introduced by Vivekanandan et al. [36] to obtain DSD parameters (N_0, μ and Λ), as

$$\begin{cases} \dfrac{M_6}{M_3} = \dfrac{N_0 \Lambda^{-(\mu+7)} \Gamma(\mu+7)}{N_0 \Lambda^{-(\mu+4)} \Gamma(\mu+4)} = \dfrac{\Gamma(\mu+7)}{\Lambda^3 \Gamma(\mu+4)} = \dfrac{(\mu+6)(\mu+5)(\mu+4)}{\Lambda^3} \\ \mu = -0.024\Lambda^2 + 1.0662\Lambda - 2.7433 \\ N_0 = \dfrac{M_6 \Lambda^{(\mu+7)}}{\Gamma(\mu+7)} \end{cases}, \quad (9)$$

where the $\mu-\Lambda$ relation is obtained from DSD observations measured by 2DVD in 2014 and 2015, using the method of Sorting and Averaging based on Two Parameters (SATP) that was described by Cao et al. [37].

PRD including Z_{H}, Z_{DR}, K_{DP}, specific horizontal attenuation (A_{H}), and specific differential attenuation (A_{DP}) are calculated from the simulated DSD with the T-matrix method. The axis ratio of raindrops is set following the experimental fit [2]; the wavelength for these calculations is set as 5.33cm, which is a typical value for C-band radar. The temperature is set to 10 Celsius degrees. The range profile of intrinsic Z_{H}, Z_{DR}, K_{DP} and ϕ_{DP} are shown in Fig. 2.

Random fluctuations, which commonly exist in measured Z_{H}, Z_{DR} and Φ_{DP}, are represented by normally distributed random noises (white noises). The standard deviations of Z_{H}, Z_{DR}, and Φ_{DP} errors are assumed to be 2 dBZ, 0.4 dB, and 5 degrees, respectively. The SNR influence on the random fluctuation is ignored for these calculations. To examine the impact of the backscattering phase caused by large raindrops or melting hail, the differential backscattering phase δ_{hv} is set to nonzero at the first K_{DP} peak in the vicinity of 28.5 km (called "bump" region), following:

$$\delta_{\mathrm{hv}}(r)=\begin{cases} \dfrac{300}{\sqrt{2\pi}\sigma_r}\exp[-\dfrac{(r-r_0)^2}{2\sigma_r{}^2}], & r_0-0.75km<r<r_0-0.75km \\ 0, & \text{else} \end{cases}, \qquad (10)$$

where σ_r is the shape parameter (is assumed to be 8 km); r is the range distance from the radar (unit [km]); and r_0 is the center of the "bump". The large "bump" with a maximal differential backscattering phase of 15.0 degrees occurs occasionally in real cases; it is used to inspect the performance of these K_{DP} estimation algorithms under this extreme situation. Finally, the intrinsic value, propagation effect, random fluctuations and "bump" effects in Φ_{DP} constitute the simulated measurements, following

$$\begin{cases} Z'_{\mathrm{H}}(k)=Z_{\mathrm{H}}(k)-2\Delta r\sum_{i=1}^{k-1}A_{\mathrm{H}}(i)+\varepsilon_{Z_{\mathrm{H}}} \\ Z'_{\mathrm{DR}}(k)=Z_{\mathrm{DR}}(k)-2\Delta r\sum_{i=1}^{k-1}A_{\mathrm{DP}}(i)+\varepsilon_{Z_{\mathrm{DR}}} \\ \Phi_{\mathrm{DP}}(k)=\phi'_{\mathrm{DP}}(k)=2\Delta r\sum_{i=1}^{k-1}K_{\mathrm{DP}}(i)+\delta_{\mathrm{hv}}+\varepsilon_{\Phi_{\mathrm{DP}}} \end{cases}, \qquad (11)$$

where the accumulation means the propagation effect of A_{H}, A_{DP}, and K_{DP}.

From Fig. 2, the whole range of the rain cell is about 60 km, with the most intense parts located from about 25 km to 40 km. The largest K_{DP} value exceeds 3 degrees per kilometer. Attenuation becomes significant, and Φ_{DP} increases rapidly through the intense parts of the rain cell. The large backscattering phase causes a large "bump" in the vicinity of the first peak of K_{DP}. For this region, it is obviously uneasy to estimate K_{DP} from Φ_{DP} because backscattering overruns the propagation effect. Nevertheless, the power measurements: Z_{H} and Z_{DR} are relatively immune from the back scattering phase as long as there is no hail. The accuracy of K_{DP} estimates from the self-consistent relation is mainly decided by the feasibility of the relation for a particular case, the random fluctuations of $Z_{\mathrm{H}} / Z_{\mathrm{DR}}$ measurements and the effect of attenuation in rain.

B. Climatological Parameters

In order to obtain the parameters for the self-consistency, the 2-year climatological DSD data from 2014 and 2015 observed by the same 2DVD as in the simulation section was used. The self-consistent relation obtained with the method documented in the previous section is shown in Fig. 3 as a scatterplot, and expressed by

$$K_{\mathrm{DP}}(Z_{\mathrm{h}}, Z_{\mathrm{dr}}) = 4.7041\mathrm{e}^{-5} Z_{\mathrm{h}}^{1.0411} Z_{\mathrm{dr}}^{-1.9097} \tag{12}$$

with $Z_{\mathrm{h}} = 10^{Z_{\mathrm{H}}/10}$ in unit of [$\mathrm{mm}^6\mathrm{m}^{-3}$] and $Z_{\mathrm{dr}} = 10^{Z_{\mathrm{DR}}/10}$ dimensionless. The scatters of intrinsic K_{DP} values, versus those estimated with Eq. (12), are distributed closely around the unity line except for several outliers. The DSDs of these outliers are dominated by a few of big drops, mainly due to the size sorting effect [38, 39] of wind shear, deviating from the standard gamma model. Even with all the different types of DSDs, the self-consistent relation of PRD exhibits great reliability and robustness. To obtain the accurate parameters in Eq. (12), all fitting procedures in this paper are performed using nonlinear methods in a linear scale instead of simple linear fitting in logarithmic scale. This is because the linear fitting in logarithmic scale would enlarge the weights of smaller data values. As there are much more light rain samples from our DSD observation, the fitting results can bias to light rain in linear fitting in logarithmic scale.

Besides the self-consistent relation among PRD, the linear coefficients of A_{H}-K_{DP} (c) and A_{DP}-K_{DP} (d) are also regressed to be utilized in attenuation correction [31], written as c=0.0987, d=0.018. The regression performance is shown in Fig. 4. With the coefficients c and d, attenuation of Z_{H}, Z_{DR} could be corrected with

$$\begin{aligned} Z_{\mathrm{H}} &= Z'_{\mathrm{H}} + c\Phi_{\mathrm{DP}}^{\mathrm{U}} \\ Z_{\mathrm{DR}} &= Z'_{\mathrm{DR}} + d\Phi_{\mathrm{DP}}^{\mathrm{U}} \end{aligned}, \tag{13}$$

in which $\Phi_{\mathrm{DP}}^{\mathrm{U}}$ means the unfolded and non-filtered differential phase, Z'_{H} and Z'_{DR} indicate attenuated measurements.

C. Comparison of Results

The K_{DP} estimations of the simulated experiment with LSF, LP, and self-consistency systems are compared in this subsection. Different lengths of adaptive range, derivative filter, and moving window for LSF, LP, and self-consistency methods, respectively, are used to illustrate the impact of these parameters to the whole system. In Fig. 5(a), the adaptive range is 2 km/27 gates for $Z_{\mathrm{H}} \geq 40$dBZ and 6 km/81 gates for $Z_{\mathrm{H}} < 40$dBZ for LSF; the derivative filter is 2 km/27 gates for LP; the moving window is 1 km/15 gates for self-consistency. A shorter moving window is used because the $Z_{\mathrm{H}}/Z_{\mathrm{DR}}$ standard deviation is much smaller than that of Φ_{DP}.

The LSF-based K_{DP} estimations have the worst performance among these three methods. Due to the "bump" effect, K_{DP} estimations have very significant fluctuations in the vicinity of this region. The peak is higher than 9 $^{\circ}$/km and the valley at the "leeside" can be lower than -3°/km. This would lead to nonphysical QPE results. Even at the positions where the intrinsic values are less than 1°/km (meaning that the slope of ϕ_{DP} is insignificant), K_{DP} estimates can still be negative. Statistical errors are not handled well in the LSF approach. When LP is used, the results are better. First, due to the non-negative constraint used, estimated K_{DP} values can never be negative even at the leeside of the "bump" region, where measured Φ_{DP} is of downward trend. This is a substantial improvement, since erroneous negative values are totally avoided. Furthermore, K_{DP} values at the windward side are also better than those obtained from the LSF method because of the constraints used in the LP approach. LP also results in better K_{DP} estimates where the rainrate is low.

Not surprisingly, the SC K_{DP} estimation results in the best outcome for this experiment. From Fig. 3, the self-consistency of PRD is very reasonable. It is fair to say that K_{DP} is not totally independent from Z_{H} and Z_{DR} when the DSDs are not absolutely different from the climatology. In Fig. 5, the difference between K_{DP} estimates from the SC method and intrinsic values are quite small, especially at the "bump" region. Differences exist only in the vicinity of the second K_{DP} peak. This is a nearly perfect result because the intrinsic self-consistency of simulated experiment PRD is almost identical to what we get from climatological DSD data (not shown), meaning that the model error is small. The main source of error is the random fluctuation, which is reduced by the moving filters. However, in other cases including real-world implementation, the model error due to the deviation of intrinsic self-consistency from the statistical relation would need to be taken into account.

Doubling the lengths of the adaptive ranges, the derivative filter and moving windows with respect to those in Fig. 5(a), we obtain another set of results, shown in Fig. 5(b). Generally, K_{DP} estimates are smoother when compared with those in Fig. 5(a). According to $\mathrm{SD}(K_{\mathrm{DP}}) = \frac{\mathrm{SD}(\Phi_{\mathrm{DP}})}{\sqrt{N(N-1)(N+1)/3}} \frac{1}{\Delta r}$, the random errors of LSF K_{DP} estimates would decrease to about 1/3 of those in Fig. 5(a) [4, 40]. Therefore, the number of negative values decreases remarkably. However, at about 24 km, the values become abnormally large. This is mainly due to the incorporation of the “bump” part of the Φ_{DP} profile when the lengths of adaptive range are enlarged. It is not surprising to see that values from LP do not show such a tendency because the consideration of the entire ray. The results from LP are also closer to the intrinsic values in the vicinity of the first peak. However, the results at the second K_{DP} peak are overly smoothed when compared with those from Fig. 5(a). The errors here are not as severe as the errors in the “bump” regions. Nevertheless, this highlights that uniform length derivative filters without additional constraints could either over-smooth the results when errors are not too severe, or under-smooth the results where Φ_{DP} measurements are too “noisy”. For this example, Z_{H} and Z_{DR} measurements are also smoother due to the increased length of the moving window in the self-consistent estimation. The results are also overly smoothed in the figure.

The intrinsic differential phase and the error part of Φ_{DP}, including random fluctuation and nonzero differential backscattering phase, are segregated in the LSF and LP methods. K_{DP} estimated from LSF and LP may deviate from the intrinsic values when the information provided by the error part dominates compared to that provided by the intrinsic differential phase. The performance of K_{DP} estimation from measured polarimetric data depends mainly on to what degree the method can extract information provided by intrinsic differential phase from the measured data: the more the useful information is contaminated by the error, the worse the performance. In most K_{DP} estimation approaches including LSF and the basic LP [17], only Φ_{DP} measurements are used. Therefore, these methods may perform worse when they are applied on the data for which the information provided by error plays a more important role. The ratio of useful information to error mainly depends on the magnitude of the error in polarimetric measurements, and the scales (for matching fixed-length filters) over which these operate. This is related to many factors such as radar hardware (e.g., antenna design, transmitter characteristics), operating parameters (e.g., pulse repetition frequency:,PRF), the propagation and scattering characteristics of the targets (e.g., Doppler spectrum characteristics), distance between targets and radar and so on. So the performance of different methods also depends on the data. Likewise, only Z_H and Z_{DR} measurements are used in the self-consistency method. However, the self-consistent relation in a specific case could deviate from the statistical one, and there are also errors in Z_H and Z_{DR} measurements. So, it is natural to combine these methods together, and to make use of as much information as possible. In the next section, we will propose a hybrid method based on the combination of the LSF, LP and self-consistent K_{DP} estimation methods.

4. A Hybrid Method on the Ideal Experiment

According to information theory [41], as more information is used in appropriate ways, variables can be more accurately determined. Under the guidance of this principle, a hybrid method using all available measurements including Z_{H}, Z_{DR}, and Φ_{DP} is proposed based on the linear programming. ρ_{hv} usually decreases when radar scans across insects or clutters, so it is usually used to identify and remove non-meteorological echoes.

As mentioned before, the SC K_{DP} estimation could obtain very accurate results when a proper moving filter is chosen. Even though model errors could cause degradation in estimation accuracy, it is revealed from Fig. 3 that self-consistent relation is very stable from a climatological perspective. In the hybrid method, the upper and lower limits for K_{DP} estimations are calculated from Z_{H}, Z_{DR} and Φ_{DP} measurements with LSF, LP and self-consistency as accurately as possible. Then, these reasonable upper and lower constraints for K_{DP} can be incorporated in the LP system. Such combinations of methods and measurements should be able to make better use of observational information and make K_{DP} estimates more accurately.

First, upper and lower limits are decided according to the upper and lower boundary shown in Fig. 3, following,

$$K_{\mathrm{DP}}^{\mathrm{U}} = C^{\mathrm{U}} \bullet K_{\mathrm{DP}}(Z_{\mathrm{h}}, Z_{\mathrm{dr}}) \\ K_{\mathrm{DP}}^{\mathrm{L}} = C^{\mathrm{L}} \bullet K_{\mathrm{DP}}(Z_{\mathrm{h}}, Z_{\mathrm{dr}}), \tag{14}$$

where $K_{\mathrm{DP}}^{\mathrm{U}} / K_{\mathrm{DP}}^{\mathrm{L}}$ and $C^{\mathrm{U}} / C^{\mathrm{L}}$ mean the upper/lower K_{DP} limits and the slope of upper/lower boundary in Fig. 3, respectively. If radome attenuation or partial beam blockage exists in real cases, there exist biases in reflectivity measurements. The biases can be corrected from LP/LSF-estimated K_{DP} using methods similar to Vivekanandan et al. [20]. The moving windows used in this example are the shorter than those used in the SC method in Fig. 5(a). Limits from Eq. (14) only use Z_{H} and Z_{DR}. In order to eliminate the potential effect of model error from the self-consistent relation or of statistical error in measurements, these limits should be further adjusted with LSF based K_{DP} estimations. LSF uses only Φ_{DP} measurements so that those estimates represent information purely independent from the self-consistent relation. In this study, heavily smoothed LSF estimations with adaptive ranges three times the length of those used in Fig. 5(a) are utilized. Adjusting the lower limits is as follows:

$$K_{\mathrm{DP}}^{\mathrm{L}} = \begin{cases} 0.5K_{\mathrm{DP}}^{\mathrm{L}} & \text{if } K_{\mathrm{DP}}^{(\mathrm{H})} < 0 \\ K_{\mathrm{DP}}^{(\mathrm{H})} & \text{if } 0 \le K_{\mathrm{DP}}^{(\mathrm{H})} < K_{\mathrm{DP}}^{\mathrm{L}} \\ K_{\mathrm{DP}}^{\mathrm{L}} & \text{if } K_{\mathrm{DP}}^{(\mathrm{H})} \ge K_{\mathrm{DP}}^{L} \end{cases}, \tag{15}$$

where heavily smoothed K_{DP} estimates from LSF are denoted as $K_{\mathrm{DP}}^{(\mathrm{H})}$. $K_{\mathrm{DP}}^{(\mathrm{H})}$ tends to underestimate K_{DP} values in heavy rain regions and overestimate those in the transition region between light rain and heavy rain. Eq. (15) would eliminate abnormally low values in the lower limits. Overestimations in $K_{\mathrm{DP}}^{(\mathrm{H})}$ would not play any role in Eq. (15). The upper limits are adjusted as follows:

$$K_{\mathrm{DP}}^{\mathrm{U}} = \begin{cases} 8, & K_{\mathrm{DP}}^{\mathrm{U}} > 8, \text{ and } Z_{\mathrm{H}} < 35\mathrm{dBZ} \\ 10, & K_{\mathrm{DP}}^{\mathrm{U}} > 10, \text{ and } Z_{\mathrm{H}} < 45\mathrm{dBZ} \end{cases} . \tag{16}$$

Information from LSF is not used here, because it is not easy to obtain stable upper K_{DP} limits without super overestimations, and severe overestimations would cause negative consequence.

The combination of the LSF and self-consistency methods results in better lower and upper limits for the K_{DP} estimation. When errors dominate in Φ_{DP} measurements, the lower limits mainly use information from Z_{H} and Z_{DR} measurements in the estimation. Similarly, the heavily smoothed LSF based K_{DP} estimates will play a role when errors in Z_{H} and Z_{DR} measurements dominate. The errors in one measurement can be ameliorated by the useful information in the other measurements.

Since more accurate limits are obtained, the next step is combining them with the LP system. Eq. (4) and (5) are modified to,

$$\mathbf{A}_{\mathrm{AUG}} = \begin{pmatrix} \mathbf{I}_n & -\mathbf{I}_n \\ \mathbf{I}_n & \mathbf{I}_n \\ \mathbf{Z}_{n-(m-1)/2,n} & \mathbf{M}_{n-(m-1)/2,n} \\ \mathbf{Z}_{n-(m-1)/2,n} & -\mathbf{M}_{n-(m-1)/2,n} \end{pmatrix}, \tag{17}$$

and,

$$\mathbf{b}_{\mathrm{AUG}} = \left(-\mathbf{b}, \mathbf{b}, \mathbf{K}_{\mathbf{DP}}^{\mathbf{L}}, -\mathbf{K}_{\mathbf{DP}}^{\mathbf{U}}\right)^T, \tag{18}$$

respectively. Now, K_{DP} constraints are controlled by the modified augmented part of $\mathbf{A}_{\mathrm{AUG}}$ and $\mathbf{b}_{\mathrm{AUG}}$, which can be written as $\mathbf{K}_{\mathbf{DP}}^{\mathbf{L}} \le \mathbf{M}_{n-(m-1)/2,n}\mathbf{x} \le \mathbf{K}_{\mathbf{DP}}^{\mathbf{U}}$, instead of simplified monotonicity constraints (nonnegative K_{DP}) used in the original LP method.

We call this approach a hybrid method, not only because it is the combination of the equations of the LSF, LP and self-consistency methods, but also for blending the underlying philosophy for each of them. The LSF is the most straightforward method. It can result in a satisfactory K_{DP} estimation when the error in the measurements does not dominate. The LP method is a global optimization algorithm for ϕ_{DP}. However, the basic methods implemented to shorter wavelengths lack some detailed consideration for K_{DP} estimation realities, especially when the error in Φ_{DP} overruns the useful information. The self-consistency method previously designed for partial beam blockage and other corrections capitalizes better on other available information (Z_{H} and Z_{DR}). This self-consistency approach often fails in critical situations such as hail cores where these methods must rigidly adhere to consistency relationship constraints that do not apply.

The proposed hybrid method and the original LP method are applied on the simulated data to show the changes in the performance (Fig. 6). The derivative filters are set as 2 km in length for both. There is only a marginal difference between ϕ_{DP} estimates from the two methods when taking an overall view of whole radial data. K_{DP} estimated by the hybrid method is smoother and much closer to intrinsic K_{DP}, owing to the more accurate constraints from the additional information. As described before, the lower the ratio of information provided by the intrinsic differential phase and the error, the more difficult it is to find solutions close to the intrinsic variables. The difference between solutions estimated by the hybrid method and the original LP method reaches a maximum at the "bump" region where the information ratio is the lowest. In the "bump" regions, minor useful information is provided by Φ_{DP} measurements, so constraints play relatively important roles. When the LP method is used without additional constraints, the nonnegative constraints associated with the cost function (of minimizing difference between measured and filtered differential phase) would make ϕ_{DP} increase quickly along with the upward slope part of the 'bump' region as shown by the red line in Fig. 6(a), and then increase slowly in the remaining part of the "bump". This would result in abnormally large K_{DP} values in the upward slope part and abnormally low K_{DP} values in the remaining part. When additional information is used as upper and lower constraints in this hybrid method, K_{DP} is limited by stricter constraints than the simpler nonnegative constraint. We see that upper and lower constraints from extra Z_H and Z_{DR} measurements result in a better estimation than simple non-negative physical constraints.

5. Verification With A Real Case

The Nanjing University-C-band-Polarimetric Radar (NJU C-POL) is a mobile C-band polarimetric radar for weather research, jointly designed by Nanjing University and Beijing Metstar Radar Company in China. Its main parameters are listed in Table 1. During the 2014-2015 field campaign of Observation, Prediction, and Analysis of severe

Convection of China (OPACC) , NJU C-POL was deployed in Anhui province, East China, to observe the summer severe convection (Fig. 1). An absolute calibration using a metallic ball was conducted to guarantee the accuracy of $Z_{\mathrm{H}} / Z_{\mathrm{V}}$ before the observations. A vertically pointing scan was also performed every 6-minute volume scan for Z_{DR} calibration. The distance between NJU C-POL and 2DVD is 171 km. These two instruments are influenced by the same synoptic systems. Therefore, it is acceptable to use DSD data collected by the 2DVD as representative to fit a statistical self-consistent relation for NJU C-POL for application of the hybrid method on the measured PRD.

An event during the Intensive Observing Period 8 (IOP8) on July 11-12, 2014 is selected for investigation from the OPACC dataset. In order to show the performance on the real event, the LSF/LP/hybrid K_{DP} methods will be applied on a plane position indication (PPI) scan. Then, quantitative precipitation estimations from three sets of LSF, LP and hybrid-based K_{DP} estimators will be compared with accumulated rainfall (AR) observed by several automatic weather stations (AWS) within the observing umbrella of the radar. QPEs are estimated according to the R - K_{DP} relation obtained from the 2DVD [8, 42], as shown in Fig. 4.

Radar scans at 1.5 degree instead of the lowest elevation (0.5 degree) are used to avoid the impact of partial beam blockages. The quality of radar moment data are carefully controlled with five procedures before estimating ϕ_{DP} and K_{DP}:

1) Z_{H} is calibrated according to the absolute calibration experiment.

2) Systematic differential phase in measured Φ_{DP} and Z_{DR} bias are removed with data from the vertical pointing scan.

3) The echoes having ρ_{hv} less than 0.75 or spectral width is larger than 9 m/s are considered as nonmeteorological or second trip echo and thus removed.

4) A much stricter constraint is used to deal with Φ_{DP} measurements that may cause errors. Along all radials, if the Φ_{DP} difference between two adjacent gates is larger than 40°, ρ_{hv} is less than 0.9, or the spectral width is larger than 6 m/s, the gate is flagged as a bad gate. Φ_{DP} values at these potential bad gates are removed and then refilled with the linear interpolations from the surrounding gates.

5) Finally, Φ_{DP} is unfolded, and correction for attenuation in rain for $Z_{\mathrm{H}}/Z_{\mathrm{DR}}$ fields is conducted using Eq.(13).

In order to illustrate the difference of the hybrid method and the basic LP method, a comparison of their results on a radial data from a PPI image collected by the NJU C-POL on July 11, 2014 at 2325UTC is shown in Fig. 7. As influenced by the back scattering phase and noise, the observed Φ_{DP} increases abnormally in the vicinity of 35 km, which is called a "bump" region similar to the abnormal back scattering region in the ideal case. ρ_{hv} (denoted in subplot [e]) also manifests a decreasing tendency in this region. This "bump" region lacks sufficient differential phase information, which could obviously impact the performance of both methods. Similar to the results in the ideal case, the ϕ_{DP} estimate from the LP method tends to increase rapidly at the first half part of the "bump" region, and then to flatten afterwards. This result is mainly required by the algorithm to minimize the cost function. However, owing to the inclusion of physical constraints, the K_{DP} estimate from the hybrid method corresponds better with Z_{H} and Z_{DR} observations in subplots (c) and (d). It is very important to note that the frequency of the occurrence of such large "bump" features is,not very low especially in the C-/X- band radar datasets. As we tested in the real data, the inclusion of these physical constraints can obviously improve the quality of the K_{DP} estimates and rainfall estimates consequently. This will be further illustrated using the whole PPI image and QPE results.

The PPI image at the 1.5 degree elevation (Fig. 8) shows that this Meiyu precipitation has a large region of uniform stratiform precipitation with multiple embedded convections near the southern part of the system. These embedded convections cause a significant radial Φ_{DP} increase, corresponding to increased K_{DP} values. Since Φ_{DP} measurements have a large dynamic range in the image, Φ_{DP} is noisy and unsuitable for use in quantitative applications.

After quality control, K_{DP} values are estimated using the LSF method with the same adaptive ranges used in the algorithms of WSR 88D (2 km/6 km) and with LP/hybrid method with adaptive derivative filters of 27 gate lengths (2 km). Before estimating the upper and lower limits for the hybrid method, the attenuation-corrected $Z_{\mathrm{H}} / Z_{\mathrm{DR}}$ are smoothed with 15-gate moving median and mean filters. Results from the PRD are found in Fig. 9. The most obvious difference of LSF based K_{DP} estimates and LP/hybrid based ones are that, with nonnegative constraints in the LP method and self-consistent constraints in the hybrid method, negative K_{DP} values completely disappear. Negative K_{DP} values are associated with localized errors. As proposed by Ryzhkov and Zrnić [8] , QPE biases could be partially mitigated by including these negative rainrates associated with negative K_{DP} values. However, if the AR is not calculated over a sufficiently large spatiotemporal area to capture both negative and positive K_{DP} estimates, this may still result in a negative rainfall accumulation. Results of LP estimation seem to be much more capable than those from LSF estimation, with erroneous negatively values disappearing. However, as shown in Fig. 10(c) and (d), the original LP based K_{DP} estimates near echo edges occasionally spike if backscatter phase contributions and filter length choices are not well-handled. The results look improved in K_{DP} estimates using the hybrid method constraints as in Fig. 10(a) and (b) for those edge regions. Around the regions of embedded convection, where Φ_{DP} measurements would likely increase more rapidly, there are additional azimuthal discontinuities in the K_{DP} image from the lesser constrained LP method than that from the better constrained hybrid method. This azimuthal discontinuity (e.g., one not the direct result of rain microphysics) indicates a potential drawback for lesser-constrained LP methods. In the meantime, having more realistic physical constraints under the proposed hybrid method, K_{DP} estimates seem to be more physically realistic and smoother.

Within 80 km radius of the NJU C-POL radar station, there are 10 AWS locations with rain gauge measurements (positions as shown in Fig. 1). The distances between AWSs and the radar are listed in Table 2. ARs from these AWSs are sampled at 1-minute temporal resolution. Since the AWSs have much shorter sampling times than the radar (approximately 6 minutes), this allows a quantitative comparison at the radar observation scale temporal resolution. The total AR results for each AWS during this event are located in Table 3. Most of the sites record moderate rainfall to heavier rainfall, with the largest 48-hour accumulated rainfall recorded as 72.8 mm.

In order to quantify the precision of K_{DP} from the LSF/LP/hybrid methods, time series, $K_{\mathrm{DP}}(i), 1 \le i \le N$, over the AWSs' sites are extracted from estimates over the entire event from UTC 02:20, July 11, 2014 to UTC 23:50, July 12, 2014. With these estimated K_{DP} time series, three sets of rainrate series are estimated using the following formula:

$$R(i) = 30.81\left|K_{\mathrm{DP}}(i)\right|^{0.775} \mathrm{sign}[K_{\mathrm{DP}}(i)], 1 \le i \le N, \tag{19}$$

where $R(i)$ is the rainrate at the i^{th} scan. The parameters of Eq. (19) are estimated from the same dataset as in Fig. 3. The scattergram of the fitting result is shown in Fig. 4. Then, the AR for each station is estimated following:

$$AR(i) = \begin{cases} R(i-1)\Delta t(i), & 2 \le i \le N \\ 0, & i = 1 \end{cases}, \tag{20}$$

where $\Delta t(i)$ is the time interval between the i^{th} and $i+1^{\mathrm{st}}$ scan over the station. It is important to note that these time series report at the highest temporal resolution we can obtain from the radar. Next, AWS observations and radar estimates are compared at five different temporal resolutions, including 1) at the radar scan time; 2) every 15 minutes; 3) every 30 minutes; 4) every 60 minutes; and 5) every 180 minutes. Here, the time series at the coarser temporal resolution reflect integrations of those at the finest temporal resolution.

Correlation coefficients and relative errors, whose formulas are:

$$\rho = \frac{\sum_{i=1}^{N}[AR_{\text{AWS}}(i) - \overline{AR_{\text{AWS}}}][AR_{\text{radar}}(i) - \overline{AR_{\text{radar}}}]}{\sqrt{\sum_{i=1}^{N}[AR_{\text{AWS}}(i) - \overline{AR_{\text{AWS}}}]^2 \sum_{i=1}^{N}[AR_{\text{radar}}(i) - \overline{AR_{\text{radar}}}]^2}}, \tag{21}$$

$$\varepsilon_{\text{r}} = \frac{\sqrt{\frac{1}{N}\sum_{i=1}^{N}[AR_{\text{AWS}}(i) - AR_{\text{radar}}(i)]^2}}{\frac{1}{N}\sum_{i=1}^{N} AR_{\text{AWS}}(i)}, \tag{22}$$

where AR_{AWS} and AR_{radar} are accumulated rainfall time series of a particular temporal resolution, and "$\bar{\ }$"denotes expected value, are listed in Table 3. The relative error represents to what degree the estimates deviate from the AWS observations. The AWS total ARs and K_{DP} based estimates are also listed to show the absolute bias.

From the table, performance varies from station to station. These differences are because of several factors, including different sampling volume/time between the radar and AWSs, and the variability of precipitation when falling (e.g., as related to microphysical or dynamical processes). Not surprisingly, radar-estimated accumulated rainfall from all three methods is in better agreement with AWS observations at the coarser temporal resolutions. In general, estimates from the hybrid method correlate better with the AWS observations than do those from the basic LP method and the LSF approach. Once again, differences between the methods are less noticeable at coarser temporal resolution. Typically, rainfall comparisons between radar and in-situ gauge measurements are produced at a temporal resolutions of 1 hour or longer (e.g., 24-hour daily accumulation mapping) to reduce the role of instantaneous measurement noise [2, 3, 42]. At such longer temporal resolutions, we find that correlation coefficients between the AR series and AWS observations are high, with most of them exceeding 0.95. It can be seen from Table 3 that, even when the comparisons are made at the highest temporal resolution (radar scan time), the majority of the correlation coefficients between the AR time series and AWS observations are larger than 0.8. Additional information from Z_{H} and Z_{DR} included in the hybrid method makes such precise rainfall estimation possible. In contrast, the LSF method shows a significant deficiency. Most sets of rainfall estimates from the LSF method have an extremely low correlation coefficients with AWS observations. Relative errors, which denotes a relative magnitude of bias, still decrease when the comparison is conducted at a coarser temporal resolution. Finally, rainfall estimates from the hybrid method exhibit a lower bias than those from the other methods.

Not surprisingly, a mismatch of the radar data and estimation methods, as well as errors associated with the AWS observations, would cause the differences between radar estimated rainfall and AWS observations. Three time series traces from AWS observations (stations 58320, 58323 and 58224) and their corresponding radar rainfall estimates are selected to help illustrate the reasons associated with 1) the LSF method under-performing as compared to the hybrid method; 2) rainfall estimations from all methods performing poorly; and 3) rainfall estimations from all three methods performing well. These time series examples to follow are all reporting at the native radar scan time interval.

To begin, Figure 11 confirms that only those time series K_{DP} estimates from LSF methods report negative values. The underlying philosophy for including negative rainfall is that effect of erroneous negative K_{DP} values would be eliminated when spatial integration is calculated (as LSF methods would also promote compensating positive

K_{DP} excursions); in other words, spatial integration of K_{DP} values estimated from LSF method would be close to the intrinsic value. If negative K_{DP} values (along a radial or along adjacent radials) are abandoned or absolute values are used, spatial integration would be positively biased. However, for these examples, time series performances over point locations are considered instead of wider spatial integrations. These negative rainfall values from the LSF would therefore be strongly decorrelated with the time series of the real precipitation. Fig. 11(a) highlights one example when the correlation coefficient of the LSF method-based rainfall estimates with AWS observations for station 58320 is near 0, implying these estimates are strongly uncorrelated. For this station example, the peak of AR observations is not very large compared with the other two subplots. The magnitude of the oscillation of the LSF method-based rainfall estimates exceeds the peak of AR observations. This means that the statistical noise resulting from the raw measurements and the processing algorithm totally contaminates the useful information.

For the LP method, the exclusion of extreme negative or positive excursion values makes the K_{DP} series correlations align closer to the intrinsic ones. However, the LP method cannot accurately recover K_{DP} at the "bump" regions with only its basic constraint configuration. Thus, we find that the extra physical constraints from Z_{H} and Z_{DR} have a positive effect for the hybrid method-estimated K_{DP}/rainfall time series. Overall, the hybrid method does a superior job when compared with the LSF and LP methods. For example, in the vicinity of index 12, both the rainfall estimates from LSF and LP predict two phantom peaks of AR, which do not match with the observations or the results from the hybrid method. The best performance in terms of total accumulation estimation is found for station 58323, where the total AR from hybrid method is almost equal to that from the observations.

However, despite the accurate AR estimate over longer scales for the hybrid method, the station 58323 example highlights other sources for the possible failure of all three methods at shorter scales including: 1) the phantom peak of AR in the vicinity of index 8, 2) the insufficient AR in the vicinity of index 12, and 3) the time shift of the main rainfall peak. As noted before, temporal mismatch issues are often related to mismatches between the height of the radar volume and the surface AWS station. This offset could be associated with instantaneous measurement errors from additional storm advection, or drop distribution evolution. Several of these storm evolution factors may be offset if our comparisons are conducted over a coarser temporal resolution. For example, the correlation coefficients exceed 0.8 for all methods once we consider 1-hour accumulations; the hybrid method-based AR reaches 0.98 for station 58323. For station 58224, the two AR peaks at index 38 and 60 are estimated successfully by all methods, thus we are able to achieve decent correlation coefficients at both the high and coarse temporal resolutions across all methods.

Finally, it should be mentioned that the comparisons performed at station 58321 were unexpectedly poor. The relative error (correlation coefficient) is extremely high (low), even when the comparison is conducted at the lengthier temporal scales, with emphasis on the LSF method-based AR performance. The total LSF method-based AR is -9.86 mm and a negative 48-hour AR is clearly not acceptable. As previously noted, spatiotemporal integration would potentially eliminate most detrimental effects of instantaneous LSF negative and positive value excursions. In general, our results still confirm the expectation that the longer the K_{DP} time series, the more likely we would find a result for the total AR close to the intrinsic value. In this example, the number of radar samples during the 48 hour window is approximately 394, which is still insufficient to offset those negative values. Both the LP and hybrid methods perform poorly, but the hybrid method-estimated total ARs still suggest the lowest biases.

In general, the hybrid method performs better than the LSF/LP methods when applied to a real event, especially when quantitatively compared verified with AWS observations.

6. Discussion and Summary

To examine the performance of K_{DP} estimators for polarimetric radar measurements, least square fitting, which is the most common operational method; linear programming, which is a newly proposed optimization approach to guarantee the nonnegativity of K_{DP} estimates; and the self-consistency, which is commonly used to calibrate radar, are compared using simulated data. Each of these methods have weaknesses when dealing with PRD that are severely affected by measurement or model error.

To improve K_{DP} estimation by efficiently utilizing different information, a hybrid method of combining LSF K_{DP} estimation and self-consistent property of polarimetric variables into the linear programming problem as stricter constraints has been developed.

This hybrid method is applied on an ideal case and on a real event to demonstrate its theoretical advantage and realistic performance. The advantage of the hybrid method is that it utilizes as much information into the estimation system as possible. The results of the ideal case and the real event suggest that it performs better than the three existing methods.

A specific method to calculate lower and upper K_{DP} limits from Z_{H} and Z_{DR} has been adopted. With these physical constraints, K_{DP} values that are too small would not exist in heavy rain areas, and K_{DP} values that are too large would not exist in light rain areas. Since the values of Z_{H} and Z_{DR} are not entirely precise (due to radial fluctuations and problems in the attenuation correction algorithm) and the method proposed is not perfect, future work could focus on obtaining more accurate lower and upper limits.

Estimating K_{DP} and ϕ_{DP} is a necessary but not sufficient part of polarimetric data quality control [43, 44]. Errors exist in polarimetric measurements mainly because of defective radar hardware, random fluctuation, clutter environment, imperfect signal processing, attenuation of hydrometeors on high frequency radar, and so on. Even if the quality of radar hardware and observing environment is ensured, and signal processing algorithms are improved, errors still exist in measured polarimetric variables (e.g., Z_{H}, Z_{DR}, ρ_{hv} and Φ_{DP}). Hybrid K_{DP} estimation method is based on optimal estimation theory, in which Z_{H}, Z_{DR} and Φ_{DP} information are [43] utilized to optimize ϕ_{DP} and K_{DP}. Future work could focus on taking measurement errors into account in the optimization to further improve the estimation performance.

Acknowledgements: This work was primarily supported by the National Fundamental Research 973 Program of China (2013CB430101) and the National Natural Science Foundation of China (grant 41475015, 41275031 and 41322032), and Program for New Century Excellent Talents in University of China. We would also like to acknowledge the work of the investigators and operators of NJU C-POL and other instruments. This manuscript has also been authored by an employee of Brookhaven Science Associates, LLC under Contract No. DE-AC02-98CH10886 with the U.S. Department of Energy. The publisher by accepting the manuscript for publication acknowledges that the United States Government retains a non-exclusive, paid-up, irrevocable, world-wide license to publish or reproduce the published form of this manuscript, or allow others to do so, for United States Government purposes.

Table 1 Settings and parameters of NJU C-POL and its observations.

Parameters	**NJU C-POL （mobile）**
Transmitter	5.625 GHz （klystron）
PRF	1000 Hz
Pulse width	0.5 μs
Peak Power	> 250 kW
Receiver	Simultaneous Horizontal/Vertical
Noise figure	< 3 dB（H and V channel）
Dynamic range	> 95 dB
Antenna feeder	paraboloid， center feed
Antenna gain	> 41 dB
Antenna aperture	3.2 m
Beam width	1.2°
Sidelobe	< -40 dB (> 15°)
Polarimetric mode	Simultaneously transmit and receive H and V
Scanning mode	PPI: 0-360° rotating speed: ~15°s^{-1} time for VCP: ~6min
Elevations	0.5, **1.5**, 2.4, 3.4, 4.3, 5.3, 6.2, 7.5, 8.7,10.0, 12.0, 14.0, 16.7, 19.5, **90.0**
Precision	
Radial resolution	75m
Radar variables	Z_{H}, Z_{DR}, ρ_{hv}, Φ_{DP}, v_{r}, σ_{v}, SNR
Z_{H} precision	1 dB
v_{r} precision	1 m/s
σ_{v} precision	1 m/s
Z_{DR} precision	0.2 dB
Φ_{DP} precision	2°

Table 2 AWSs positions and their distances away from NJU C-POL. The first line stands for the names of the AWSs.

Station Name	**58221**	**58225**	**58212**	**58215**	**58220**	**58224**	**58311**	**58320**	**58321**	**58323**
Lon.	117.30	117.67	116.77	116.78	117.15	117.02	116.50	117.13	117.30	117.48

Lat.	32.85	32.533	32.717	32.433	32.467	32.65	31.73	31.733	31.78	31.88
Dis.	77.09	65.73	68.45	42.30	32.73	53.62	75.68	48.83	46.75	46.44

Table 3 Comparison of the accumulated rainfall AR from AWS units to those estimated from LSF/LP/hybrid methods. Information on these AWS stations is shown in Table 2.

Station Name			**58221**	**58225**	**58212**	**58215**	**58220**	**58224**	**58311**	**58320**	**58321**	**58323**
Total AR.		aws	39.70	42.80	44.30	40.40	39.90	36.90	72.80	21.90	26.60	41.80
		LSF	13.16	27.98	55.36	52.14	46.98	45.14	61.35	19.60	-9.86	24.31
		LP	35.20	34.12	44.97	57.30	69.75	43.42	57.05	29.35	26.78	36.70
		HY	38.47	34.95	53.39	53.09	63.51	46.52	65.63	23.06	23.33	41.45
CORR. COEF.	**Rad.**	LSF	0.41	0.45	0.42	0.52	0.41	0.66	0.51	0.00	0.19	0.31
		LP	0.60	0.56	0.73	0.72	0.57	0.89	0.57	0.48	0.34	0.48
		HY	0.75	0.66	0.88	0.83	0.71	0.94	0.61	0.81	0.60	0.39
	15 min	LSF	0.74	0.60	0.76	0.68	0.63	0.69	0.64	0.21	0.22	0.50
		LP	0.85	0.73	0.95	0.83	0.77	0.90	0.66	0.61	0.53	0.66
		HY	0.92	0.83	0.98	0.89	0.89	0.95	0.72	0.90	0.79	0.51
	30 min	LSF	0.80	0.78	0.88	0.77	0.70	0.75	0.65	0.20	0.31	0.79
		LP	0.89	0.83	0.98	0.88	0.84	0.90	0.67	0.70	0.71	0.87
		HY	0.95	0.91	0.98	0.94	0.91	0.95	0.72	0.93	0.87	0.80
	60 min	LSF	0.85	0.90	0.85	0.80	0.76	0.75	0.94	0.24	0.20	0.86
		LP	0.93	0.91	0.96	0.92	0.89	0.91	0.94	0.84	0.77	0.91
		HY	0.95	0.96	0.98	0.96	0.93	0.97	0.97	0.97	0.88	0.98
	180 min	LSF	0.91	0.92	0.80	0.95	0.91	0.80	0.93	0.65	0.10	0.90
		LP	0.95	0.94	0.97	0.98	0.97	0.93	0.97	0.94	0.89	0.93
		HY	0.96	0.97	0.96	0.99	0.98	0.98	0.97	0.99	0.95	0.99
RELATIVE ERROR	**Rad.**	LSF	2.64	2.40	2.68	2.61	3.15	2.21	2.94	4.84	3.36	3.26
		LP	1.68	1.76	1.67	1.31	1.44	1.07	2.24	1.88	2.01	2.46
		HY	1.38	1.28	1.14	0.79	1.05	0.90	2.06	1.00	1.42	3.29
	15 min	LSF	1.52	1.66	1.47	1.46	2.17	1.40	1.74	3.26	2.72	2.20
		LP	1.21	1.22	0.75	0.91	1.09	0.79	1.52	1.57	1.60	1.65
		HY	1.06	0.89	0.51	0.63	0.75	0.64	1.34	0.83	1.20	2.30
	30 min	LSF	1.37	1.04	1.07	1.20	1.69	1.12	1.30	3.09	2.50	1.39
		LP	1.14	0.93	0.58	0.83	0.91	0.71	1.15	1.34	1.44	1.04
		HY	0.99	0.67	0.44	0.53	0.68	0.58	1.04	0.71	1.14	1.27
	60 min	LSF	0.99	0.64	0.89	1.24	1.24	1.00	0.59	2.39	2.45	1.31
		LP	0.68	0.58	0.53	0.85	0.74	0.65	0.51	1.07	1.31	1.07
		HY	0.60	0.45	0.41	0.53	0.6	0.49	0.36	0.53	1.09	0.64

180 min	LSF	0.95	0.50	0.69	1.01	0.76	0.88	0.50	1.69	2.43	1.06
	LP	0.61	0.46	0.32	0.83	0.55	0.67	0.35	0.83	1.02	0.73
	HY	0.57	0.34	0.34	0.48	0.47	0.55	0.33	0.37	0.81	0.35

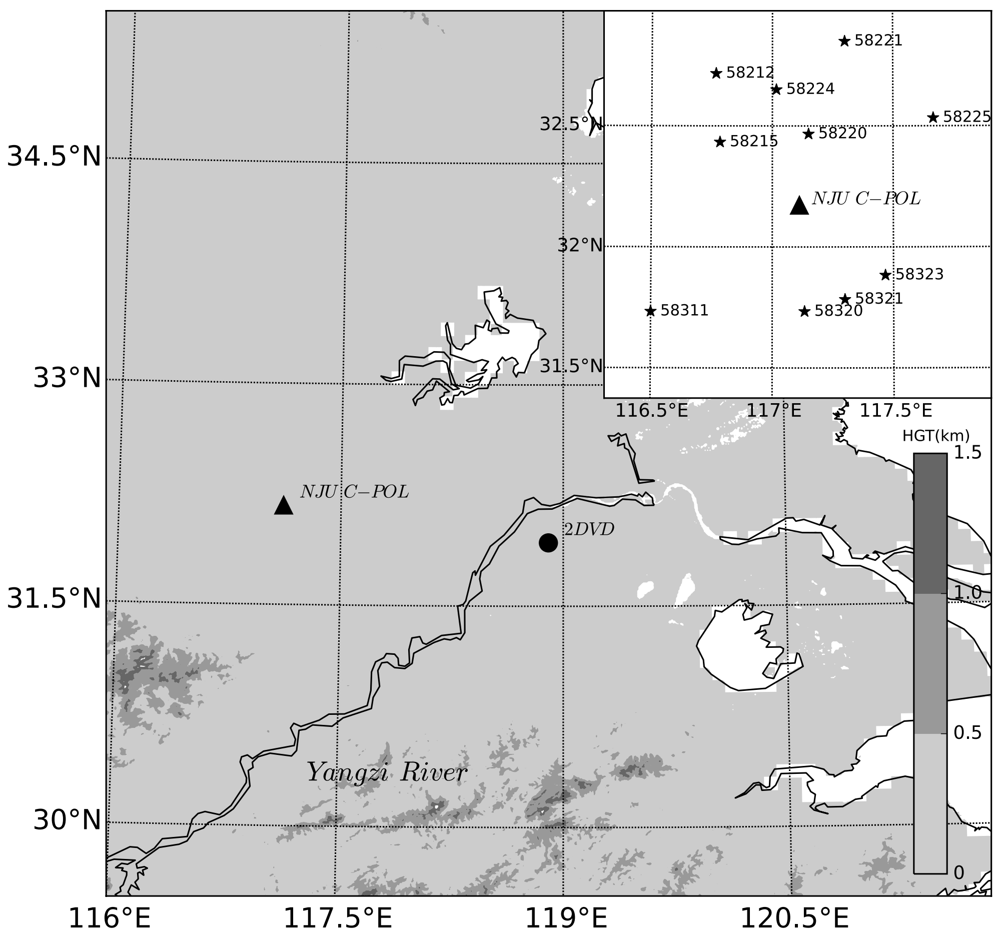

Figure 1: Location and topography of Yangzi-Huaihe river basin and instruments sites. The black triangle and circle indicate NJU C-POL, 2DVD, respectively. Black pentagrams in the smaller subplot indicate AWS locations.

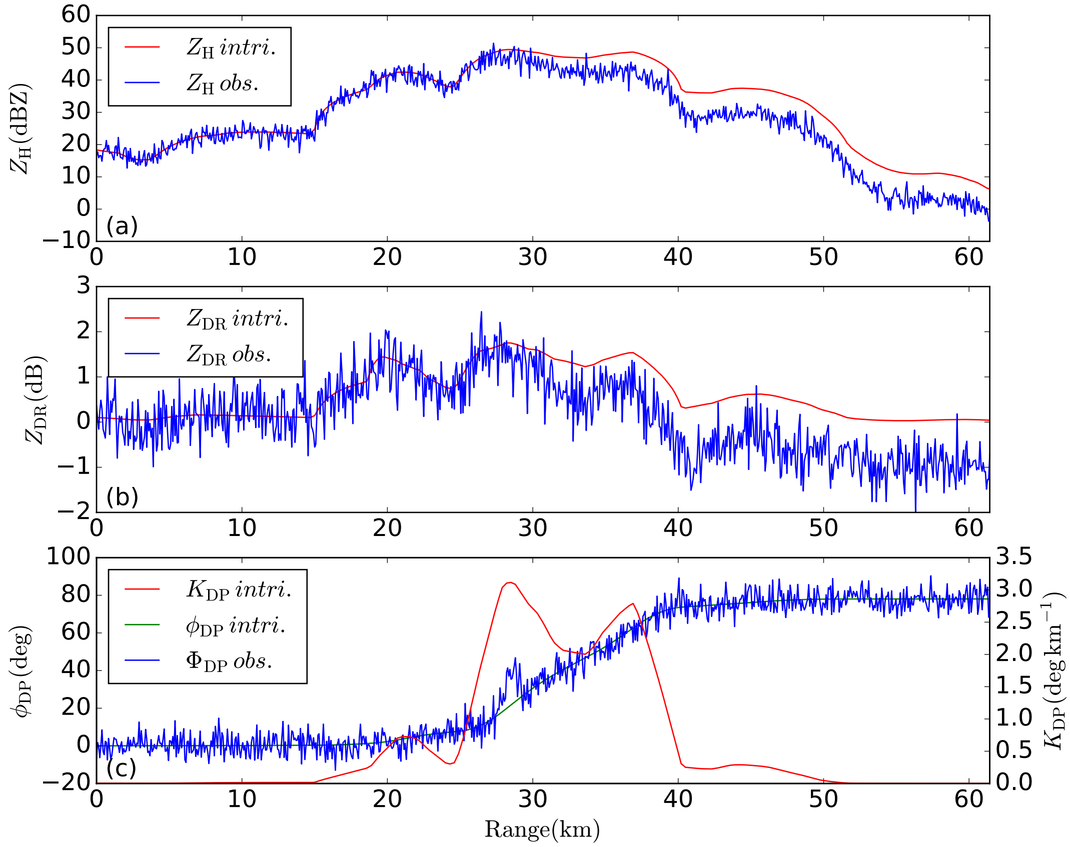

Figure 2: Range profile of polarimetric variables from simulated DSDs. (a) intrinsic Z_{H} (red solid line) and Z_{H} observation (blue solid line); (b) intrinsic Z_{DR} (red solid line) and Z_{DR} observation (blue solid line); (c) intrinsic K_{DP} (red solid line) , Φ_{DP} observation (blue solid line), and intrinsic ϕ_{DP} (green solid line).

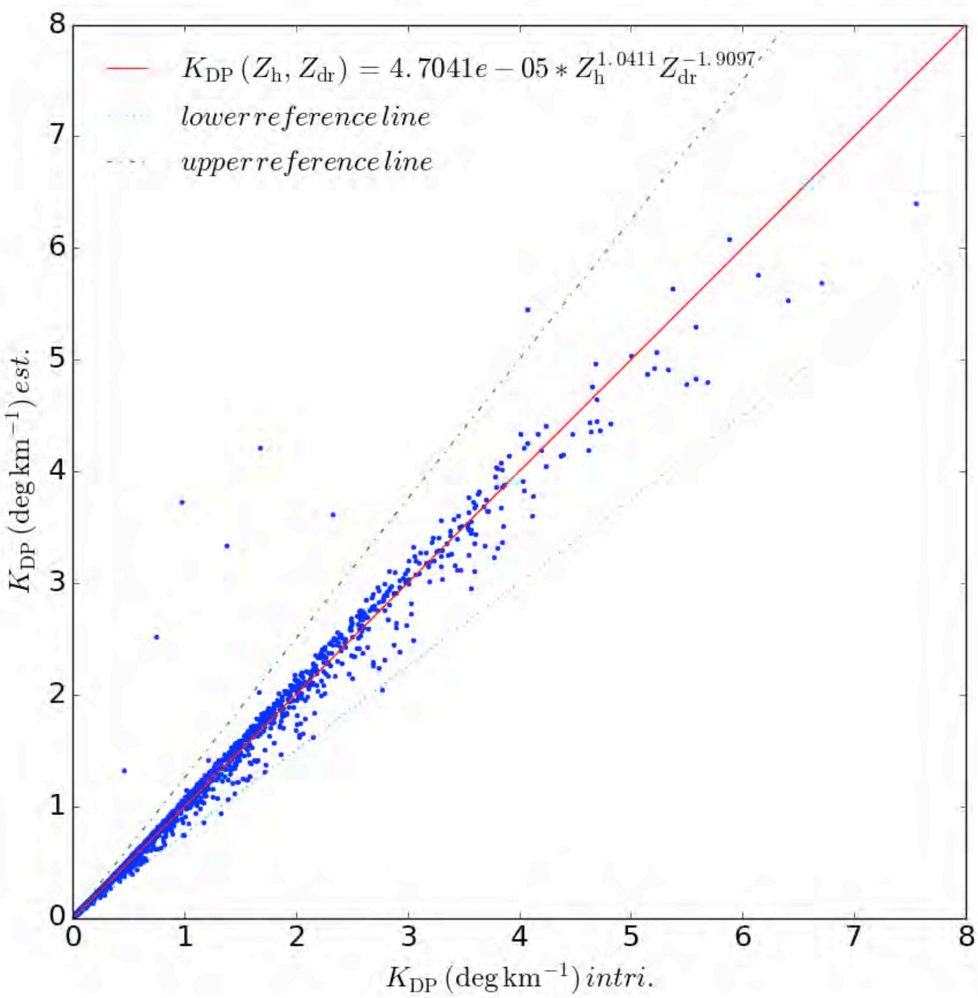

809
Figure 3: Scattergram of simulated K_{DP} directly from 2DVD observation vs. K_{DP} estimation from Z_H and Z_{DR} using a self-consistency relation. The DSD data used was collected by 2DVD denoted in Fig.1 from 2014 to 2015. The green dot dash line and cyan dot line are upper [$125\%K_{DP}(Z_H, Z_{DR})$] and lower [$75\%K_{DP}(Z_H, Z_{DR})$] reference lines.

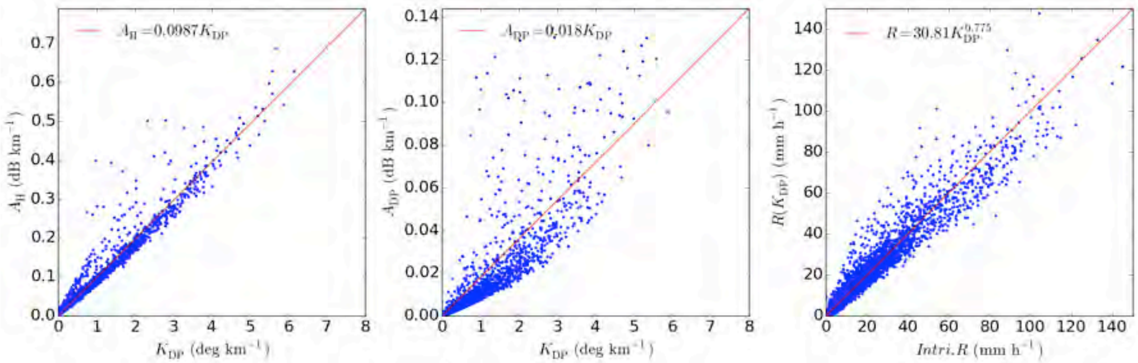

Figure 4: Specific attenuation (A_H : left) and specific differential attenuation (A_{DP} : middle) versus specific differential phase (K_{DP}) for C-band, as well as the calculated intrinsic rainrate versus that estimated from K_{DP} .

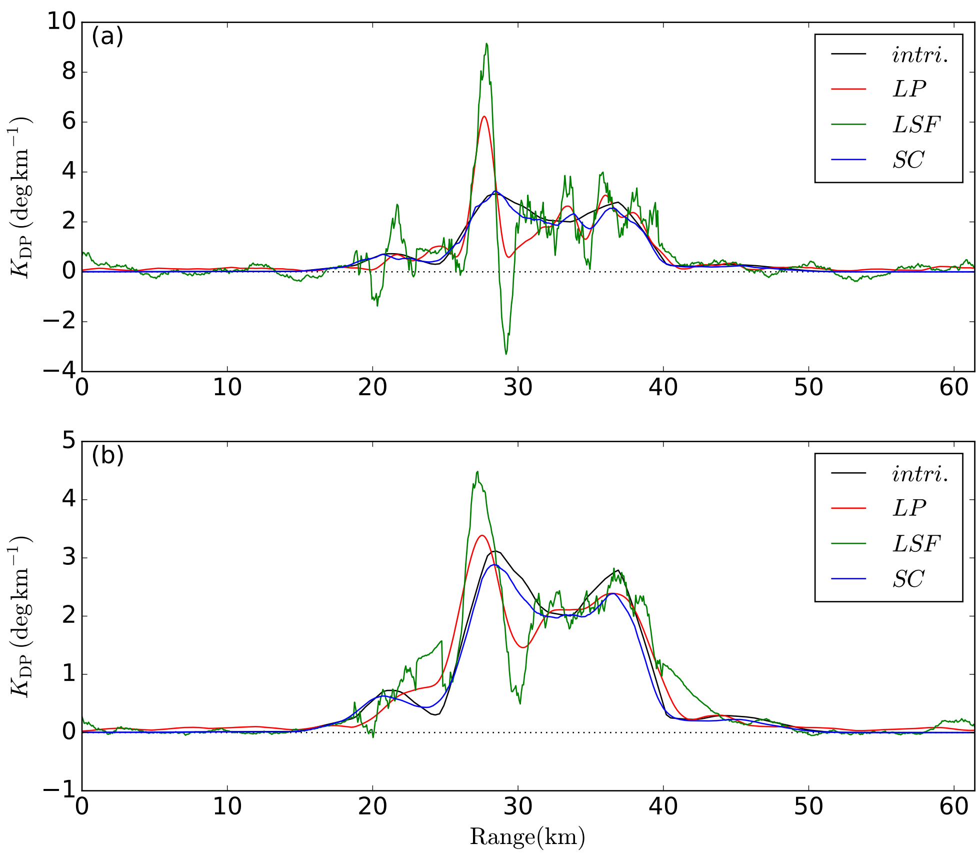

Figure 5: Comparisons of K_{DP} estimations from the LSF (green solid), LP (red solid) and self-consistency (blue solid) methods with two different lengths of adaptive ranges/derivative filters/moving windows. Shorter (2 km) options as in (a), longer (6 km) options as in (b). The intrinsic K_{DP} is denoted with black solid line.

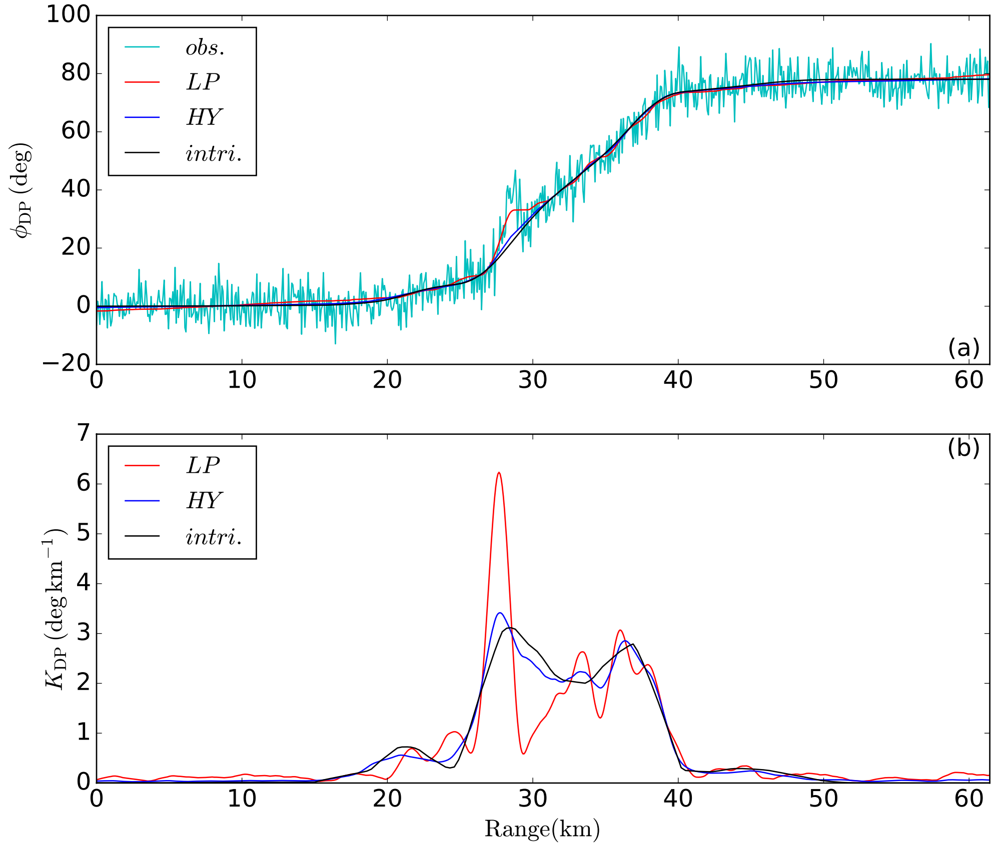

Figure 6: Comparisons of ϕ_{DP} (a)/ K_{DP} (b) estimates from the hybrid (blue solid) and basic linear programming (red solid) methods. Simulated Φ_{DP} observations are denoted as cyan solid line in (a). The intrinsic ϕ_{DP} / K_{DP} values are denoted with black solid lines.

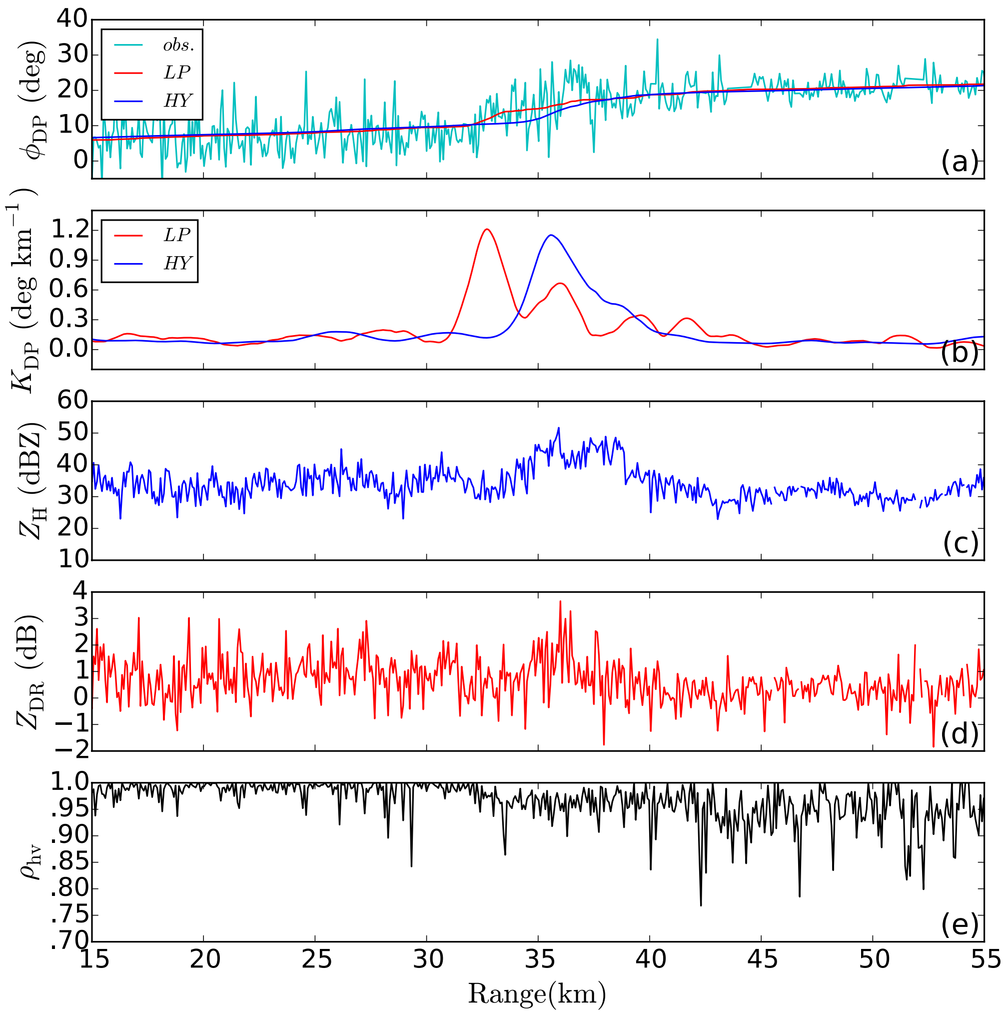

Figure 7: Comparisons of ϕ_{DP} (a)/ K_{DP} (b) estimates from hybrid (blue solid) and basic linear programming (red solid) methods applied on a ray collected by NJU C-POL on July 11, 2014 at 2325UTC at an elevation of 1.5 degrees and azimuth of 54.33 degrees. Φ_{DP} observations are denoted as cyan solid line in (a). The attenuation corrected Z_H (blue solid), attenuation corrected Z_{DR} (red solid) and corrected ρ_{hv} (black solid) are denoted in subplots (c), (d) and (e).

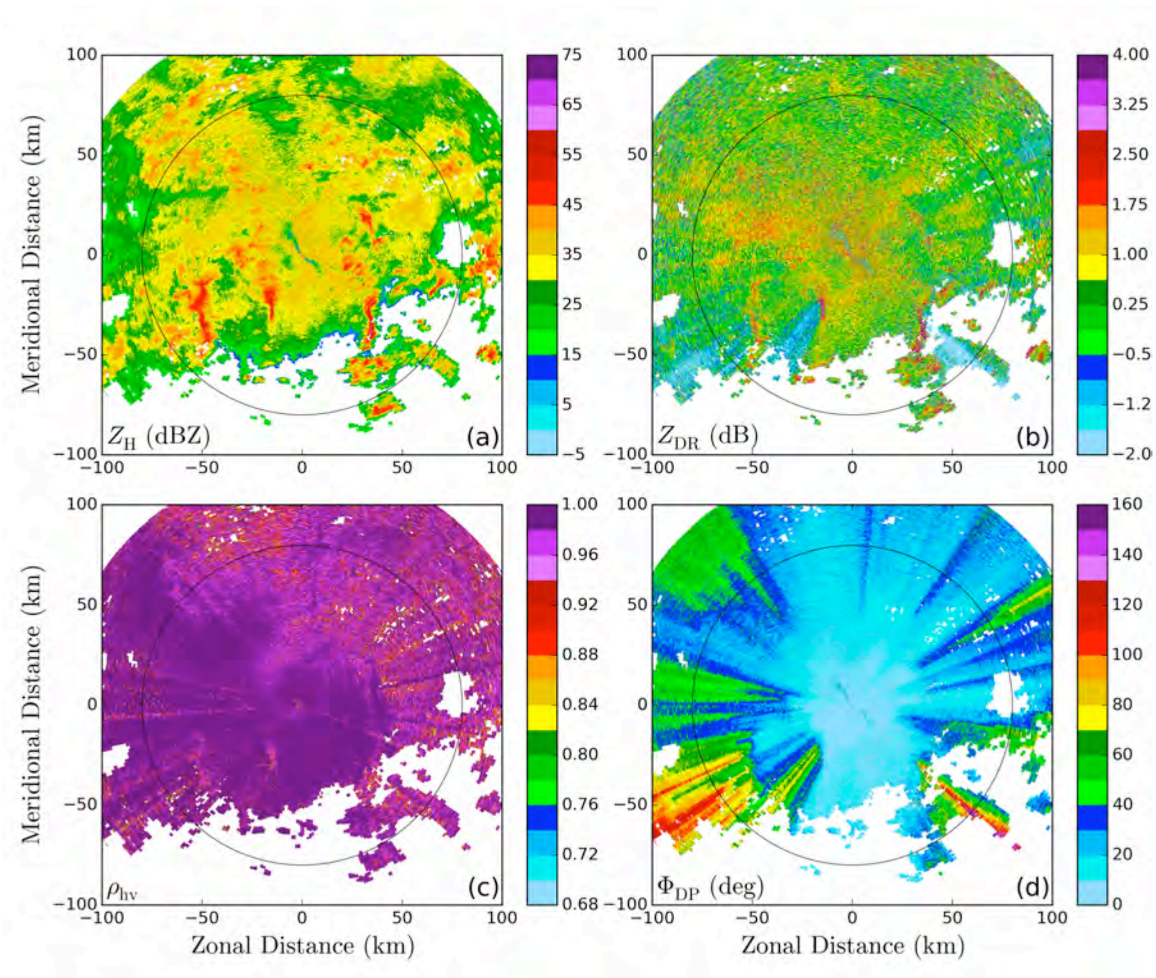

Figure 8: Quality controlled PRD images of a Meiyu precipitation event collected by NJU C-POL on July 11, 2014 at 2325 UTC at an elevation angle of 1.5 degrees. (a) $Z_{\mathrm{H}}(\mathrm{dBZ})$, (b) $Z_{\mathrm{DR}}(\mathrm{dB})$, (c) ρ_{hv}, and (d) $\Phi_{\mathrm{DP}}(\mathrm{deg})$.

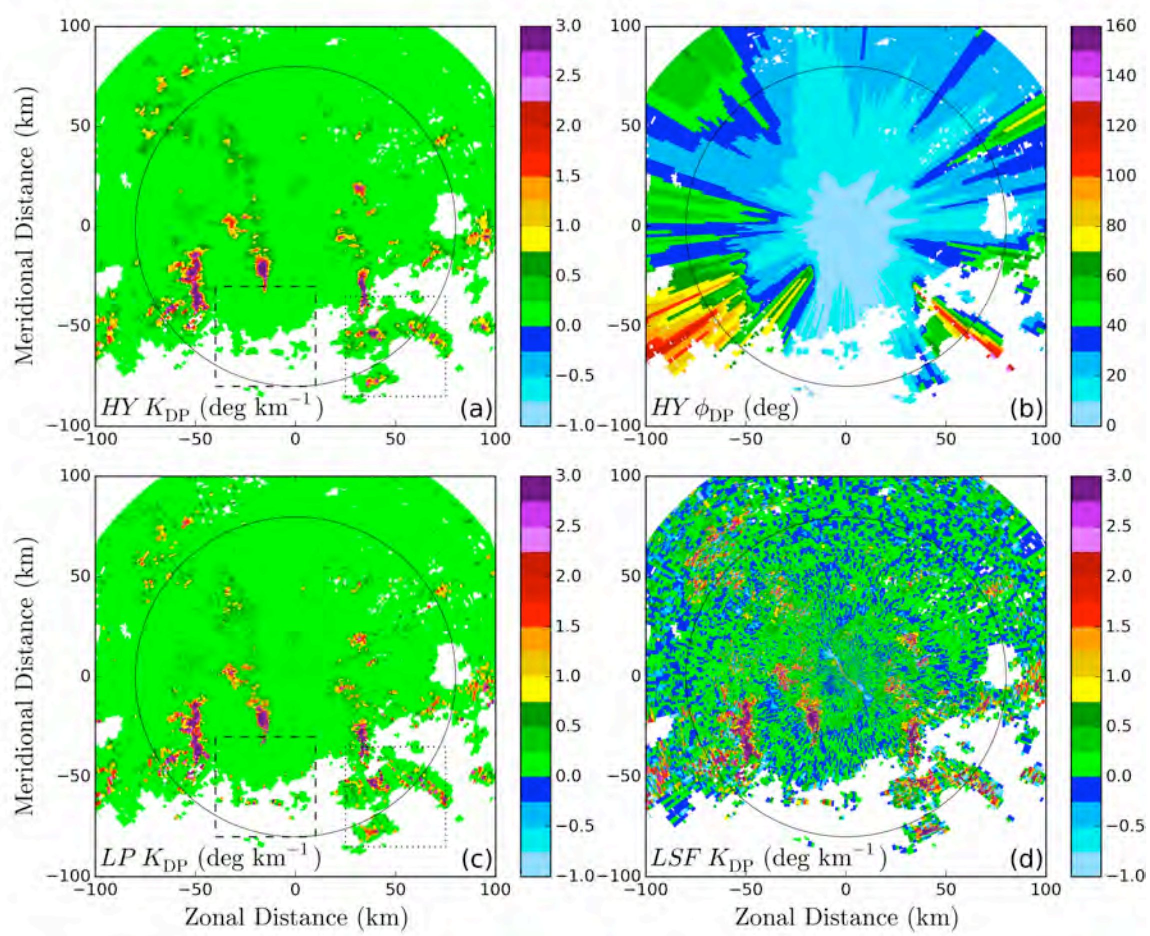

Figure 9: Comparison of K_{DP}/ϕ_{DP} estimation based on NJU C-POL data shown in Fig. 8. (a) K_{DP} estimates from hybrid method, (b) ϕ_{DP} estimates from hybrid method, (c) K_{DP} estimates from the basic LP method, (d) K_{DP} estimates from LSF method. The black circles are reference lines at a radius of 80 km from the radar. Regions denoted by dashed and dotted rectangles are enlarged in Fig. 10.

824

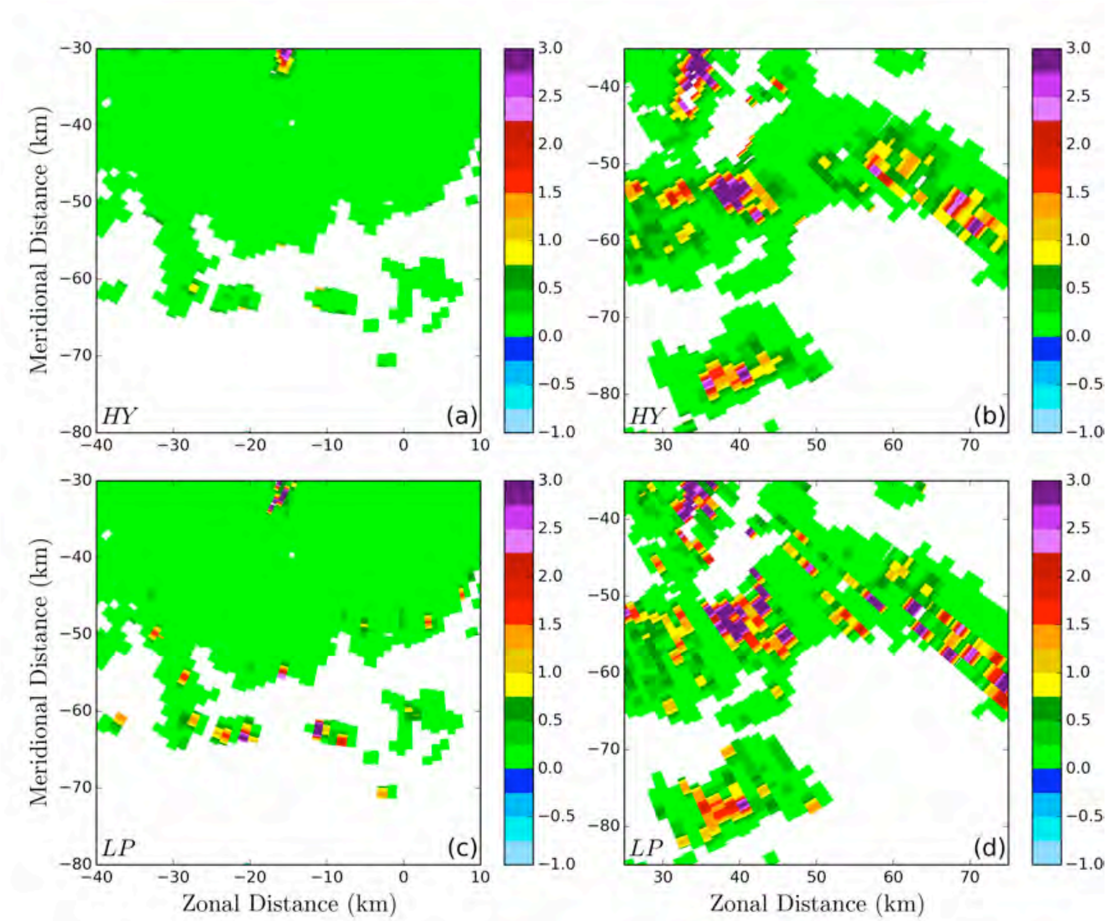

Figure 10: Zoom in for K_{DP} images shown in Fig. 9. Region of (a)/(b) is corresponding to the dashed/dotted rectangle in Fig. 9(a); region of (c)/(d) is corresponding to the dashed/dotted rectangle in Fig. 9(c).

825

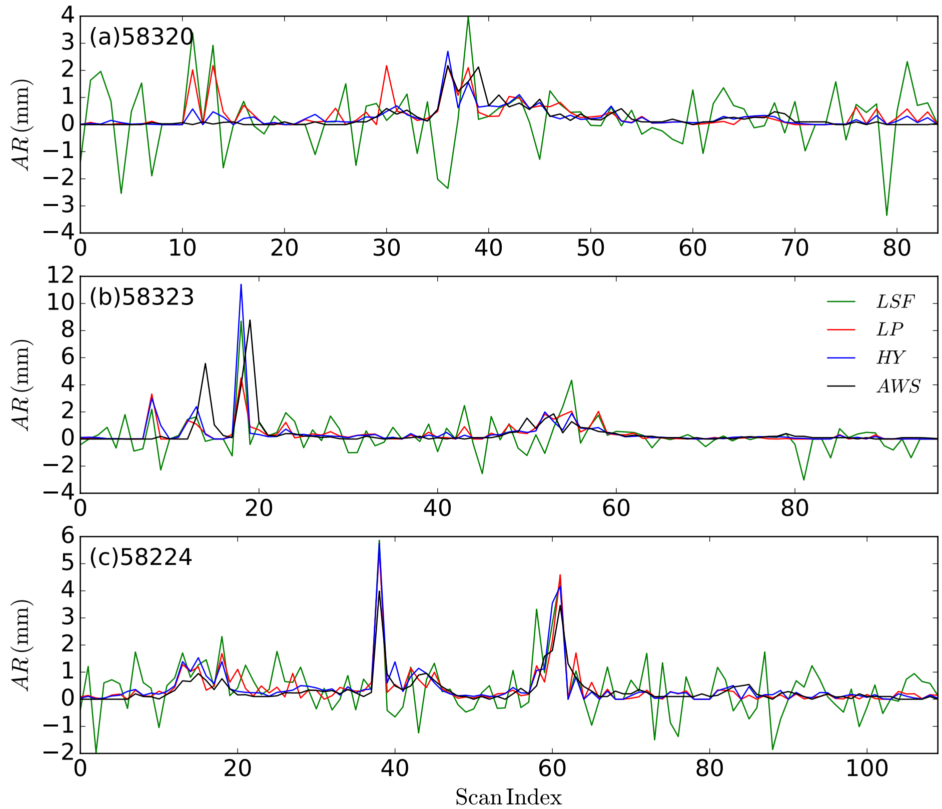

Figure 11: Time series of accumulated rainfall estimated from K_{DP} of LSF (green solid lines), LP (red solid lines), and hybrid (blue solid lines) methods and corresponding AWS observations at station (a) 58320, (b) 58323, (c) 58224.

Reference

[1] Q. Cao, M. B. Yeary, and G. Zhang, "Efficient ways to learn weather radar polarimetry," *Education, IEEE Transactions on,* vol. 55, pp. 58-68, 2012.

[2] E. A. Brandes, G. Zhang, and J. Vivekanandan, "Experiments in Rainfall Estimation with a Polarimetric Radar in a Subtropical Environment," *Journal of Applied Meteorology,* vol. 41, pp. 674-685, 2002/06/01 2002.

[3] A. V. Ryzhkov, S. E. Giangrande, and T. J. Schuur, "Rainfall estimation with a polarimetric prototype of WSR-88D," *Journal of Applied Meteorology,* vol. 44, pp. 502-515, Apr 2005.

[4] V. Bringi and V. Chandrasekar, *Polarimetric Doppler weather radar: principles and applications*: Cambridge University Press, 2001.

[5] H. S. Park, A. V. Ryzhkov, D. S. Zrnić, and K.-E. Kim, "The Hydrometeor Classification Algorithm for the Polarimetric WSR-88D: Description and Application to an MCS," *Weather and Forecasting,* vol. 24, pp. 730-748, 2009/06/01 2009.

[6] A. V. Ryzhkov and D. S. Zrnic, "Polarimetric Rainfall Estimation in the Presence of Anomalous Propagation," *Journal of Atmospheric and Oceanic Technology,* vol. 15, pp. 1320-1330, 1998/12/01 1998.

[7] A. Ryzhkov and D. Zrnic, "Beamwidth Effects on the Differential Phase Measurements of Rain," *Journal of Atmospheric and Oceanic Technology,* vol. 15, pp. 624-634, 1998/06/01 1998.

[8] A. Ryzhkov and D. Zrnić, "Assessment of Rainfall Measurement That Uses Specific Differential Phase," *Journal of Applied Meteorology,* vol. 35, pp. 2080-2090, 1996/11/01 1996.

[9] J. Hubbert and V. N. Bringi, "An Iterative Filtering Technique for the Analysis of Copolar Differential Phase and Dual-Frequency Radar Measurements," *Journal of Atmospheric and Oceanic Technology,* vol. 12, pp. 643-648, Jun 1995.

[10] J. Hubbert, V. Chandrasekar, V. N. Bringi, and P. Meischner, "Processing and Interpretation of Coherent Dual-Polarized Radar Measurements," *Journal of Atmospheric and Oceanic Technology,* vol. 10, pp. 155-164, Apr 1993.

[11] Z. Hu and L. Liu, "Applications of wavelet analysis in differential propagation phase shift data de-noising," *Advances in Atmospheric Sciences,* vol. 31, pp. 825-835, Jul 2014.

[12] M. Schneebeli, J. Grazioli, and A. Berne, "Improved Estimation of the Specific Differential Phase Shift Using a Compilation of Kalman Filter Ensembles," *Ieee Transactions on Geoscience and Remote Sensing,* vol. 52, pp. 5137-5149, Aug 2014.

[13] M. Istok, M. Fresch, Z. Jing, S. Smith, R. Murnan, A. Ryzhkov*, et al.*, "WSR-88D dual polarization initial operational capabilities," in *Preprints, 25th Conf. on International Interactive Information and Processing Systems (IIPS) for Meteorology, Oceanography, and Hydrology, Phoenix, AZ, Amer. Meteor. Soc*, 2009.

[14] J. Vivekanandan, G. Zhang, and M. Politovich, "An assessment of droplet size and liquid water content derived from dual-wavelength radar measurements to the application of aircraft icing detection," *Journal of Atmospheric and Oceanic Technology,* vol. 18, pp. 1787-1798, 2001.

[15] E. A. Brandes, "Dual-polarization radar fundamentals and algorithm prospects," *Report on Next Generation Weather Radar Program–Operational Support Facility, WSR-88D Commerce-Defence-Transportation,* 2000.

[16] J. Testud, E. Le Bouar, E. Obligis, and M. Ali-Mehenni, "The Rain Profiling Algorithm Applied to Polarimetric Weather Radar," *Journal of Atmospheric and Oceanic Technology,* vol. 17, pp. 332-356, 2000/03/01 2000.

[17] S. E. Giangrande, R. McGraw, and L. Lei, "An Application of Linear Programming to Polarimetric Radar Differential Phase Processing," *Journal of Atmospheric and Oceanic Technology,* vol. 30, pp. 1716-1729, 2013.

[18] D. Bertsimas and J. N. Tsitsiklis, *Introduction to linear optimization* vol. 6: Athena Scientific Belmont, MA, 1997.

[19] G. Scarchilli, E. Gorgucci, V. Chandrasekar, and A. Dobaie, "Self-consistency of polarization diversity measurement of rainfall," *Ieee Transactions on Geoscience and Remote Sensing,* vol. 34, pp. 22-26, Jan 1996.

[20] J. Vivekanandan, G. F. Zhang, S. M. Ellis, D. Rajopadhyaya, and S. K. Avery,

"Radar reflectivity calibration using differential propagation phase measurement," *Radio Science,* vol. 38, Mar 12 2003.

[21] S. E. Giangrande and A. V. Ryzhkov, "Calibration of dual-polarization radar in the presence of partial beam blockage," *Journal of Atmospheric and Oceanic Technology,* vol. 22, pp. 1156-1166, Aug 2005.

[22] C. D. Rodgers, *Inverse methods for atmospheric sounding: theory and practice* vol. 2: World scientific Singapore, 2000.

[23] Y. Wang and V. Chandrasekar, "Algorithm for Estimation of the Specific Differential Phase," *Journal of Atmospheric and Oceanic Technology,* vol. 26, pp. 2565-2578, 2009/12/01 2009.

[24] R. G. Bland, "New finite pivoting rules for the simplex method," *Mathematics of Operations Research,* vol. 2, pp. 103-107, 1977.

[25] W. L. Winston, M. Venkataramanan, and J. B. Goldberg, *Introduction to mathematical programming* vol. 1: Thomson/Brooks/Cole, 2003.

[26] E. Jones, T. Oliphant, and P. Peterson, "{SciPy}: Open source scientific tools for {Python}," 2014.

[27] S. E. Giangrande, S. Collis, A. K. Theisen, and A. Tokay, "Precipitation Estimation from the ARM Distributed Radar Network during the MC3E Campaign," *Journal of Applied Meteorology and Climatology,* vol. 53, pp. 2130-2147, 2014/09/01 2014.

[28] M. I. Mishchenko, L. D. Travis, and D. W. Mackowski, "T-matrix computations of light scattering by nonspherical particles: A review," *Journal of Quantitative Spectroscopy & Radiative Transfer,* vol. 55, pp. 535-575, May 1996.

[29] J. Vivekanandan, W. M. Adams, and V. N. Bringi, "Rigorous Approach to Polarimetric Radar Modeling of Hydrometeor Orientation Distributions," *Journal of Applied Meteorology,* vol. 30, pp. 1053-1063, 1991/08/01 1991.

[30] J. Y. Gu, A. Ryzhkov, P. Zhang, P. Neilley, M. Knight, B. Wolf*, et al.*, "Polarimetric Attenuation Correction in Heavy Rain at C Band," *Journal of Applied Meteorology and Climatology,* vol. 50, pp. 39-58, Jan 2011.

[31] V. Bringi, V. Chandrasekar, N. Balakrishnan, and D. Zrnic, "An examination of propagation effects in rainfall on radar measurements at microwave frequencies,"

Journal of Atmospheric and Oceanic Technology, vol. 7, pp. 829-840, 1990.

[32] L. D. Carey, S. A. Rutledge, D. A. Ahijevych, and T. D. Keenan, "Correcting propagation effects in C-band polarimetric radar observations of tropical convection using differential propagation phase," *Journal of Applied Meteorology,* vol. 39, pp. 1405-1433, Sep 2000.

[33] A. V. Ryzhkov, S. E. Giangrande, V. M. Melnikov, and T. J. Schuur, "Calibration Issues of Dual-Polarization Radar Measurements," *Journal of Atmospheric and Oceanic Technology,* vol. 22, pp. 1138-1155, 2005/08/01 2005.

[34] G. Zhang, J. Vivekanandan, and E. Brandes, "A method for estimating rain rate and drop size distribution from polarimetric radar measurements," *Ieee Transactions on Geoscience and Remote Sensing,* vol. 39, pp. 830-841, Apr 2001.

[35] C. W. Ulbrich, "Natural Variations in the Analytical Form of the Raindrop Size Distribution," *Journal of Climate and Applied Meteorology,* vol. 22, pp. 1764-1775, 1983.

[36] J. Vivekanandan, G. Zhang, and E. Brandes, "Polarimetric Radar Estimators Based on a Constrained Gamma Drop Size Distribution Model," *Journal of Applied Meteorology,* vol. 43, pp. 217-230, 2004/02/01 2004.

[37] Q. Cao, G. Zhang, E. Brandes, T. Schuur, A. Ryzhkov, and K. Ikeda, "Analysis of Video Disdrometer and Polarimetric Radar Data to Characterize Rain Microphysics in Oklahoma," *Journal of Applied Meteorology and Climatology,* vol. 47, pp. 2238-2255, 2008/08/01 2008.

[38] D. T. Dawson, E. R. Mansell, Y. Jung, L. J. Wicker, M. R. Kumjian, and M. Xue, "Low-Level ZDR Signatures in Supercell Forward Flanks: The Role of Size Sorting and Melting of Hail," *Journal of the Atmospheric Sciences,* vol. 71, pp. 276-299, 2014/01/01 2013.

[39] M. R. Kumjian and A. V. Ryzhkov, "The Impact of Size Sorting on the Polarimetric Radar Variables," *Journal of the Atmospheric Sciences,* vol. 69, pp. 2042-2060, 2012/06/01 2012.

[40] E. Gorgucci, G. Scarchilli, and V. Chandrasekar, "Specific Differential Phase Estimation in the Presence of Nonuniform Rainfall Medium along the Path," *Journal of Atmospheric and Oceanic Technology,* vol. 16, pp. 1690-1697,

1999/11/01 1999.

[41] C. E. Shannon, "A mathematical theory of communication," *ACM SIGMOBILE Mobile Computing and Communications Review,* vol. 5, pp. 3-55, 2001.

[42] S. E. Giangrande and A. V. Ryzhkov, "Estimation of Rainfall Based on the Results of Polarimetric Echo Classification," *Journal of Applied Meteorology and Climatology,* vol. 47, pp. 2445-2462, 2008/09/01 2008.

[43] K. Friedrich, M. Hagen, and T. Einfalt, "A quality control concept for radar reflectivity, polarimetric parameters, and Doppler velocity," *Journal of Atmospheric and Oceanic Technology,* vol. 23, pp. 865-887, Jul 2006.

[44] D. A. Marks, D. B. Wolff, L. D. Carey, and A. Tokay, "Quality Control and Calibration of the Dual-Polarization Radar at Kwajalein, RMI," *Journal of Atmospheric and Oceanic Technology,* vol. 28, pp. 181-196, Feb 2011.